PCCP

PAPER

View Article Online
View Journal | View Issue

Check for updates

Cite this: *Phys. Chem. Chem. Phys.*, 2025, **27**, 18741

Competition between electron transfer and reactive capture in ion–molecule reactions at low collision energies: isotopic and stereodynamic effects in the reactions of CH_3F with H_2^+, HD^+ and D_2^+

Raphaël Hahn, †‡[a] David Schlander, ‡[a] Jeremy O. Richardson, [a]
Timothy P. Softley [b] and Frédéric Merkt *[acd]

Received 16th April 2025,
Accepted 6th August 2025

DOI: 10.1039/d5cp01466b

rsc.li/pccp

The bimolecular reactions between CH_3F and H_2^+, HD^+ and D_2^+ have been studied in the range of collision energies between ∼0 and $k_B \times 30$ K using a merged-beam approach. The ion–molecule reactions were investigated following photoexciting of H_2 (HD, D_2) to high Rydberg states in a supersonic beam, merging the Rydberg-molecule beam with a cold supersonic beam of CH_3F using a surface-electrode Rydberg–Stark deflector and monitoring the CH_3^+, CH_2F^+ and CH_3F^+ ions generated by the reactions of H_2^+ (HD^+, D_2^+) with CH_3F within the distant orbit of the Rydberg electron. In all three reaction systems, a strong increase of the rate coefficients was observed at collision energies below $k_B \times 4$ K. Branching ratios for the formation of CH_3^+, CH_2F^+ and CH_3F^+ were measured for all three reactions as a function of the collision energy. The branching ratio for the formation of CH_3^+ was found to decrease with increasing deuteration of the hydrogen molecular ion and to increase at collision energies below $k_B \times 4$ K. The experimental results were interpreted using model calculations based on a rotationally adiabatic capture model as well as using classical trajectory simulations. The reaction products are shown to be generated in two distinct mechanisms: electron transfer leading to a dominant CH_2F^+ and a weaker CH_3F^+ product channel, and short-range complex formation leading predominantly to CH_3^+ by F^- transfer, with a weaker contribution of CH_2F^+ by H^- transfer. The model calculations highlight the role played by quantum-statistical and stereodynamical effects associated with the $J = 1$, $|K| = 1$ ground state of *para*-CH_3F and by the reduced mass of the colliding partners: the orientation of CH_3F molecules induced by the electric field of the ion favours the production of CH_3^+ by F^- transfer at low collision energies and the slower approach of the reaction partners with increasing reduced mass favours electron transfer at intermediate distances.

1 Introduction

Ion–molecule reactions are a driving force in the chemistry of low-density gaseous environments and play an important role in the chemistry of planetary atmospheres, interstellar molecular clouds, and dilute plasmas.[1–5] The electric field emanating from the ions can polarize neighbouring molecules, which induces a long-range attractive interaction and can initiate reactive collisions even between distant reaction partners. In experiments, the motion and internal states of molecular ions can be precisely controlled in the gas phase and ion–molecule reactions are excellent systems to investigate fundamental aspects of chemical reactivity, particularly at low temperatures.[6–12]

Ion–molecule reactions can be broadly classified in two main categories:[13–16] (i) charge-transfer (or electron-transfer) reactions $A^+ + B \rightarrow A + B^+$, sometimes followed by the fragmentation of B^+, which can be regarded as nonadiabatic processes starting on the potential-energy surface of the reactants with asymptote $A^+ + B$ and ending on the potential-energy surface of the products with asymptote $A + B^+$; and (ii) adiabatic reactions $A^+ + B \rightarrow C^+ + D$ taking place on a single

---

[a] *Department of Chemistry and Applied Biosciences, ETH Zurich, 8093 Zurich, Switzerland. E-mail: frederic.merkt@phys.chem.ethz.ch*
[b] *School of Chemistry, University of Birmingham, Edgbaston B15 2TT, UK*
[c] *Department of Physics, ETH Zurich, 8093 Zurich, Switzerland*
[d] *Quantum Center, ETH Zurich, 8093 Zurich, Switzerland*

† Present address: Laboratoire de Physique des Lasers, Université Sorbonne Paris Nord, 93430 Villetaneuse, France.

‡ These authors contributed equally to this work.

Born–Oppenheimer potential-energy surface. Over the years, a broad range of concepts and methods has been elaborated to predict the rates of ion–molecule reactions and the branching ratios for the formation of different products. Whereas adiabatic reactions can be treated within the framework of transition-state theory, the description of electron-transfer processes requires a nonadiabatic treatment. In typical ion–molecule reaction systems, electron-transfer and adiabatic reactions are in kinetic competition and understanding the factors that may favour one type of reaction over the other is important. Full-dimensional quantum-mechanical treatments yield quantitative information in this regard and have brought considerable insights in the case of reactions involving atoms and diatomic molecules (see, *e.g.*, ref. 17–21). However, these treatments rapidly become prohibitively complex and expensive with increasing number of atoms.

For many applications in astrophysics and atmospheric chemistry, the total reaction rate coefficients can be estimated using ion–molecule capture models.[1,22] In such models, thermal or state-specific capture rate coefficients k_{cap} are determined corresponding to ion–molecule trajectories representing what is known as the fall of a particle towards the centre.[23,24] This fall takes place whenever the collision energy is large enough to overcome barriers, including centrifugal barriers, in the long-range potential of the ion–molecule collision system. The fall results in the formation of a capture complex, which for exothermic barrier-free adiabatic reactions leads to the formation of products with unit probability. The theory of ion–molecule capture is fully developed and various approximations can be used, depending on the type of molecular systems and the temperature range of interest. The simplest model, introduced by Langevin,[25] considers only the long-range interaction between the charge of the ion and the induced dipole moment of the molecule and is successful in predicting the total rate of key reactions such as $H_2^+ + H_2 \rightarrow H_3^+ + H$.[18,26–28] More refined capture models consider the electric multipole moments of the molecules, and parametrized rate constants extracted from trajectory calculations[13,29,30] are broadly used. Rotationally adiabatic capture models[22,31–36] are particularly successful in predicting rate constants at low temperatures and low collision energies, as verified in an increasing number of experimental studies.[37–46] At the lowest temperatures and collision energies, capture models can be extended to include the effects of quantum scattering.[47–50] However, being restricted to the treatment of long-range interactions, capture models are usually considered to be unsuitable for predicting branching ratios for competing processes taking place at short range[22,51] although there are notable exceptions: for neutral–neutral reactions capture theory has been combined with statistical treatments as in ref. 52 to enable prediction of branching ratios. In the case of the $O^+(^4S)$ + HD reaction, Dateo and Clary have shown that the displacement of the centre of mass from the centre of polarization introduces a torque which preferentially exposes the H side of HD to the O^+ ion and favours the OH^+ product over the OD^+ product at low collision energies.[53]

In the present article, we report on the investigation of the competition between electron-transfer and adiabatic reactions at low collision energies in the range below $k_B \times 30$ K, using as examples the reactions between rotationally cold ($T_{\mathrm{rot}} \approx 5$ K) CH_3F and H_2^+ (as well as HD^+ and D_2^+), forming CH_3F^+, CH_2F^+, and CH_3^+. In this range, which corresponds to the conditions encountered in interstellar molecular clouds, hardly any kinetic energy is available to drive endothermic reactions or to overcome potential barriers separating reactants from products. The reactions taking place under these conditions are therefore almost exclusively exothermic barrier-free adiabatic reactions as well as electron-transfer reactions $A^+ + B \rightarrow A + B^+$ in which the adiabatic ionization energy of B is less than that of A. The observation in the present work of significant energy-dependent isotopic effects in the branching ratios for the formation of the three ion products leads to the conclusion that, at low collision energies, electron transfer competes with F^- and H^- atom transfer. This reaction system thus provides an ideal opportunity to investigate this competition and to link the observed branching ratios and energy-dependent rate coefficients to state-specific stereodynamical effects resulting from the orientation of the dipolar CH_3F molecule induced by the field of the ion. To anticipate the main conclusions of this investigation, the importance of electron transfer is found to increase with the degree of deuteration of the molecular hydrogen ion and with increasing collision energy. Somewhat unexpectedly, the main trends observed experimentally can be explained, at least in part, by capture theory, in contrast to the general belief that capture theories cannot be used for that purpose.

Several previous studies of ion–molecule reactions involving CH_3F have been reported and helped us rationalizing our findings: Chau and Bowers have reported total rate constants for the reaction of CH_3F with the rare gas ions and several molecular ions and found charge transfer to be the dominant process in most cases. They interpreted their results in terms of the Franck–Condon factors for ionization of the fluoromethane molecules.[54] Tsuji *et al.* have used a flowing-afterglow apparatus coupled with a low-pressure chamber to measure product-ion distributions and rate constants in the charge-transfer reactions between Ar^+ and CH_3F. The dominant product was found to be CH_2F^+, although CH_3^+, CH_2^+ and CHF^+ were also observed as minor products.[55] Willitsch *et al.* reported collision-energy-dependent rate coefficients for the reaction between Ca^+ and CH_3F in the range between $k_B \times 2.6$ K and 3.2 K and observed a decrease of the rate coefficient with increasing collision energy.[56] Zhelyazkova *et al.* measured the collision-energy dependence of the total rate coefficient of the $He^+ + CH_3F$ reaction between ~ 0 and $k_B \times 10$ K observing the CH_2^+, CF^+ and CHF^+ products, and reported a strong increase below $k_B \times 1$ K.[40] Okada *et al.* reported a decrease of the capture rate constant of the $Ca^+ + CH_3F$ reactions with increasing rotational temperature of CH_3F at collision energies down to $k_B \times 30$ K.[57] In a related study, Jankunas *et al.* have investigated the Penning-ionization reaction between metastable neon and CH_3F at low collision energies in a merged-beam apparatus and observed that the branching ratios for the production of the CH_3F^+, CH_3^+ and CH_2F^+ ions are independent of the collision energy down to about $k_B \times 120$ mK.[58] Finally, the fragmentation dynamics of CH_3F^+ following threshold photoionization of CH_3F has been characterized in a series of detailed studies using synchrotron radiation and coincidence methods,[59–61] extending earlier experimental[62–66] and theoretical[67,68] studies of the fragmentation dynamics of CH_3F^+.

2 Experimental setup and methods

The reactions between CH_3F and H_2^+ (HD^+, D_2^+) were investigated at low collision energies using the Rydberg-merged-beam approach described in detail in earlier publications.[38,45] In this approach, one observes the ion–molecule reactions between the H_2^+ (HD^+, D_2^+) ion core of Rydberg states of principal quantum number $n \approx 30$ and the CH_3F molecules in their ground vibronic state. At these n values, the ion–molecule reaction takes place within the large Rydberg-electron orbit and is not affected by the distant Rydberg electron, as demonstrated experimentally.[38,69–71] The Rydberg electron, however, protects the reacting cations from being accelerated by stray electric fields, which is essential to reach low collision energies. The measurement of the collision-energy dependence of the ion–molecule reaction rate coefficient relies on the use of two pulsed skimmed supersonic beams, initially propagating at a 10° angle, generated by home-built short-pulse valves (valve-opening duration of $\sim$20 μs, repetition rate 25 Hz), one for the neutral precursor of the ion (here H_2, HD or D_2) and one for the CH_3F molecule. The hydrogen molecules are photoexcited to low-field-seeking Rydberg–Stark states in an electric field of about 15 V cm^{-1} with the ion core in a selected rovibrational level (v^+, N^+) using the resonant three-photon excitation sequences

$$H_2\ X\ {}^1\Sigma_g^+(v=0, N=1) \rightarrow B\ {}^1\Sigma_u^+(3,2) \rightarrow I^-\ {}^1\Pi_g^-(0,2) \rightarrow n=30\ [H_2^+\ X^+\ {}^2\Sigma_g^+(0,1)] \quad (1)$$

$$HD\ X\ {}^1\Sigma_g^+(v=0, N=0) \rightarrow B\ {}^1\Sigma_u^+(4,1) \rightarrow I^+\ {}^1\Pi_g^+(0,2) \rightarrow n=31\ [HD^+\ X^+\ {}^2\Sigma_g^+(0,0)] \quad (2)$$

$$D_2\ X\ {}^1\Sigma_g^+(v=0, N=0) \rightarrow B\ {}^1\Sigma_u^+(4,1) \rightarrow I^+\ {}^1\Pi_g^+(0,2) \rightarrow n=31\ [D_2^+\ X^+\ {}^2\Sigma_g^+(0,0)]. \quad (3)$$

The ground states of *ortho*-H_2 and -D_2 are chosen because of the larger populations resulting from the spin-statistical factors. The electric field is generated between two parallel planar electrodes located near the entrance of a curved surface-electrode Rydberg–Stark deflector and accelerator.[72] This deflector is used to merge the beam of $H_2(n)$ [$HD(n)$, $D_2(n)$] Rydberg molecules with the CH_3F beam and to precisely set their mean relative velocity v_{rel}^0.

The collision-energy dependence of the rate coefficient is measured in the reaction zone, which consists of a Wiley–McLaren-type time-of-flight mass spectrometer with its ion-extraction axis perpendicular to the merged-beam-propagation axis, by monitoring the yield of ionic reaction products as a function of v_{rel}^0. The measurements are carried out under conditions where the CH_3F molecule density is much larger than the density of $H_2(n)$ [$HD(n)$, $D_2(n)$] molecules and the reaction probability of the $H_2(n)$ molecules is less than 1%. Consequently, the relative rate coefficients can be determined by normalising the product-ion signal by the densities of the $H_2(n)$ and CH_3F molecules. In our experiments, we do not measure absolute but only relative densities and therefore we can only determine relative, not absolute, values of the collision-energy-dependent rate coefficients. The relative densities are extracted from the integrated signal measured with the fast-ionization gauges for the neutral CH_3F molecules and from the integrated ion signal in the time-of-flight mass spectrum for H_2^+ (HD^+, D_2^+).

To precisely control the reaction-observation time $\tau = t_2 - t_1$, we use a sequence of two electric-field pulses (see top-right inset in Fig. 1) and only monitor the product ions generated in the field-free interval between the two pulses. The first pulse, with falling edge at t_1, rejects all ions produced before t_1 and the second pulse, with rising edge at t_2, extracts the product ions formed during the interval τ for detection. Although the product ions are initially formed within the Rydberg-electron orbit, their internal energy is high so that autoionization takes place rapidly at the n values studied ($n \approx 30$). To ensure that no product ions leave the reaction zone prior to the extraction pulse, we verify that the product-ion yield increases linearly with τ. Under these conditions ($\tau \leq 15$ μs), the slope of the increase of a given product ion with τ is directly proportional to the rate coefficient of the corresponding reaction channel. In the case of the $HD^+ + CH_3F$ reaction, a constant (τ-independent) offset of the CH_3^+ product yield was observed, probably caused by a small misalignment of the two molecular beams and leading to the production of CH_3^+ during the ion extraction after t_2.

The mean collision energy $\langle E_{coll} \rangle_i$ and its distribution $f_i(E_{coll})$ are determined at each experimental cycle (index i) from (a) time-of-flight and imaging measurements of the three-dimensional velocity distribution of the cloud of deflected $H_2(n)$ [$HD(n)$, $D_2(n)$] molecules, and (b) time-of-flight measurements of the longitudinal velocity distribution of the CH_3F molecular beam, as detailed in ref. 45. Because the size of the Rydberg-molecule cloud in the reaction zone is much smaller ($\phi \approx 1$ mm) than that of the CH_3F molecule cloud, the distribution of relative velocities between the CH_3F and the Rydberg molecules is primarily given by the transverse (x, y) velocity distributions $f_x(v_{R_x})$ and $f_y(v_{R_y})$ of the Rydberg molecules and by the distribution of longitudinal (z) relative velocities $f_z(v_{rel_z})$ at the measured mean forward velocities of the two beams. Indeed, the longitudinal dispersion of the short CH_3F gas pulse over the long (0.9 m) propagation distance between the CH_3F valve orifice and the reaction zone guarantees that only molecules within a very narrow longitudinal velocity class ($\sim\pm$15 m s^{-1}) overlap with the Rydberg-molecule cloud during the reaction-observation time. Moreover, the transverse-velocity distribution of the CH_3F molecules is limited geometrically by the size of the $H_2(n)$ cloud and the skimmers to less than $\pm$4 m s^{-1} at the typical forward velocities of the CH_3F beam ($\sim$1200 m s^{-1}).

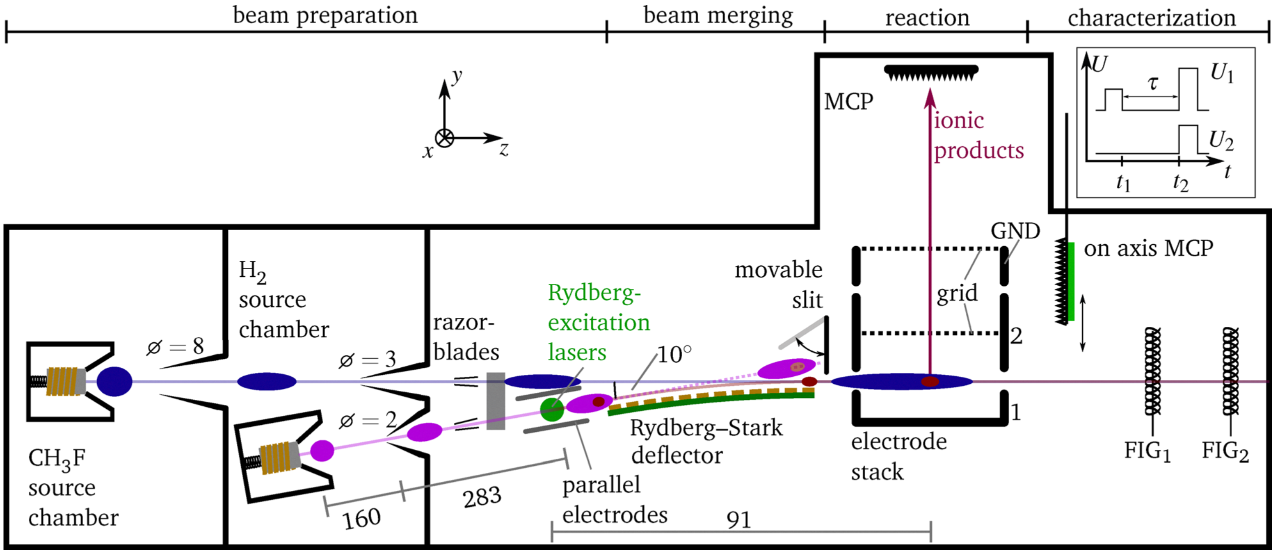

Fig. 1 Schematic representation of the experimental setup comprising supersonic-beam source chambers, a Rydberg–Stark surface-electrode deflector to merge the beams and adjust their relative velocity, and the reaction zone consisting of an ion-time-of-flight mass spectrometer. MCP = microchannel plates, FIG = fast ionization gauge, GND = ground. All dimensions are given in mm. The inset at the top right displays the electric-potential pulse sequence that is applied to the electrodes 1 and 2 of the electrode stack to extract the ions for detection. The blue, pink and red ellipsoidal shapes schematically indicate the molecular clouds of CH_3F, ground-state hydrogen and hydrogen Rydberg molecules at different positions in the merged-beam apparatus, respectively.

Overall, the experimentally determined velocity distributions are well represented by Gaussian distributions, which enables us to convert the measured three-dimensional distribution of relative velocities $f(v_{R_x}, v_{R_y}, v_{rel_z})$ into a (one-dimensional) distribution of collision energies $f(E_{coll})$. The procedure is detailed in the appendix and includes a transformation from Cartesian coordinates $(v_{R_x}, v_{R_y}, v_{rel_z})$ to spherical coordinates (v_{rel}, θ, ϕ), as illustrated in Fig. 11. This transformation reliably describes the transition between the limiting cases of $v^0_{rel} = 0$, where the collision energy is given by the relative motion in all three spatial directions (x, y, z), and $v^0_{rel} \to \infty$, where the collision energy is only given by the relative motion in the merged-beam-propagation direction (z). The resulting collision-energy distributions are well described by v^0_{rel} and their standard deviations $s_{E_{coll}}$, which are represented graphically as a function of v^0_{rel} in Fig. 2. The solid lines in Fig. 2 represent fits of the collision-energy resolution $s_{E_{coll}}$ according to the empirical expression[40]

$$s_{E_{coll}} = T_r k_B + a\sqrt{T_r k_B}\sqrt{\frac{1}{2}\mu\left(v^0_{rel}\right)^2}, \qquad (4)$$

with adjustable parameters T_r and a.

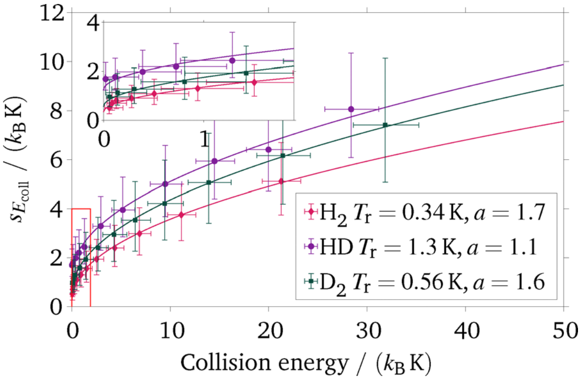

Fig. 2 Standard deviation of the collision-energy distributions as a function of the collision energy $\mu(v^0_{rel})^2/2$ for H_2, HD and D_2. The error bars correspond to indicative uncertainties of ±20 m s^{-1} and ±40 m s^{-1} in the mean value and the width of the relative velocity distribution, respectively. The inset shows the data within the red frame at low collision energies on an enlarged scale.

The different widths of the observed collision-energy distributions for the three reaction systems reflect the different reduced masses, differences in the intersection volumes of the three lasers used to excite H_2, HD and D_2 to the Rydberg–Stark states, and the relative positions of these volumes with respect to the deflector, as well as differences in the dynamics of the molecules in the moving electric traps at the surface of the deflector. In particular, the collision-energy resolution in the experiments involving HD(n) Rydberg states is slightly worse than for the experiments involving $H_2(n)$ and $D_2(n)$, which we attribute to a less efficient excitation of the HD(n) molecules that made it more difficult to optimize the experimental conditions.

Because our measurements primarily target the low-collision-energy range between 0 and $k_B \times 30$ K, the experiments are carried out under conditions where the initial velocities of both supersonic beams are similar ($\sim$1200 m s^{-1}). We operate the valves at a stagnation pressure of $\sim$3 bar. For the CH_3F beam, we use a CH_3F : Ne : He mixture with a 1 : 7 : 13 pressure ratio and heat the valve to about 380 K. Under these conditions, the vibrational motion of the CH_3F molecules in the supersonic expansion is cooled to the ground state and the rotational motion to a

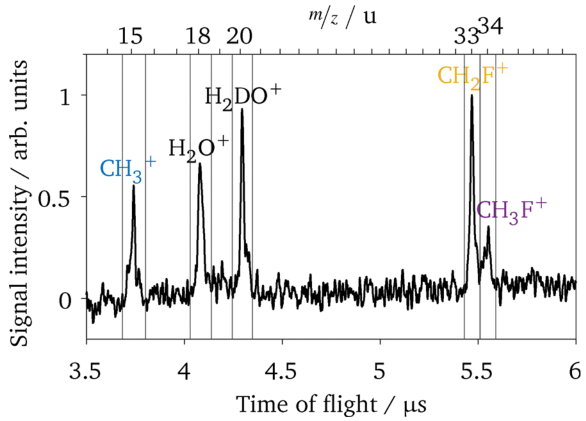

Fig. 3 Typical ion-time-of-flight mass spectrum observed for the D_2^+ + CH_3F reaction. The vertical lines represent the time-of-flight intervals over which the ion signals were integrated. The ion products labelled in black stem from reactions involving the background gas.

temperature T_{rot} of $\sim$5 K (see also Section 3). For the H_2 (HD, D_2) beams, we expand the pure gas and cool the valve to temperatures between 45 and 140 K, depending on the desired final velocity. The collision energy is then adjusted by changing the settings of the surface-electrode deflector to precisely control the mean velocity of the $H_2(n)$ [$HD(n)$, $D_2(n)$] beams.

Fig. 3 shows a typical ion-time-of-flight (TOF) mass spectrum of the D_2^+ + CH_3F reaction system recorded after a reaction-observation time of 15 μs. The experiments are carried out under single-collision conditions and the CH_3^+, CH_2F^+ and CH_3F^+ products are the only observed products for this reaction system. The remaining ions observed in the TOF spectrum, H_2O^+ and H_2DO^+, are products of the reaction of D_2^+ with H_2O molecules in the background gas. They are also observed when the CH_3F valve is either turned off or triggered so that the CH_3F gas pulse does not overlap with the $D_2(n)$ beam in the reaction zone, whereas the CH_3^+, CH_2F^+ and CH_3F^+ signals disappear in these cases. The fact that the CH_3^+, CH_2F^+ and CH_3F^+ peaks are well separated from the other masses enables us to derive the branching ratios for the formation of the different product ions from the integrated signal intensities, as discussed in more detail in Section 3. In experiments in which the magnitudes of the two electric-field pulses were varied, we verified that the product ions are generated by autoionization of the $CH_3F(n)$, $CH_2F(n)$ or $CH_3(n)$ products during the reaction-observation time, releasing the corresponding ions (CH_3F^+, CH_2F^+, or CH_3^+) and an electron.

3 Results

The relative rate coefficients and product-ion branching ratios obtained from our measurements of the reactions of CH_3F with H_2^+, HD^+ and D_2^+ are presented in the upper part of Fig. 4. The red dots with error bars represent the total product-ion yield, *i.e.*, the sum of the integrated CH_3^+, CH_2F^+ and CH_3F^+ ion

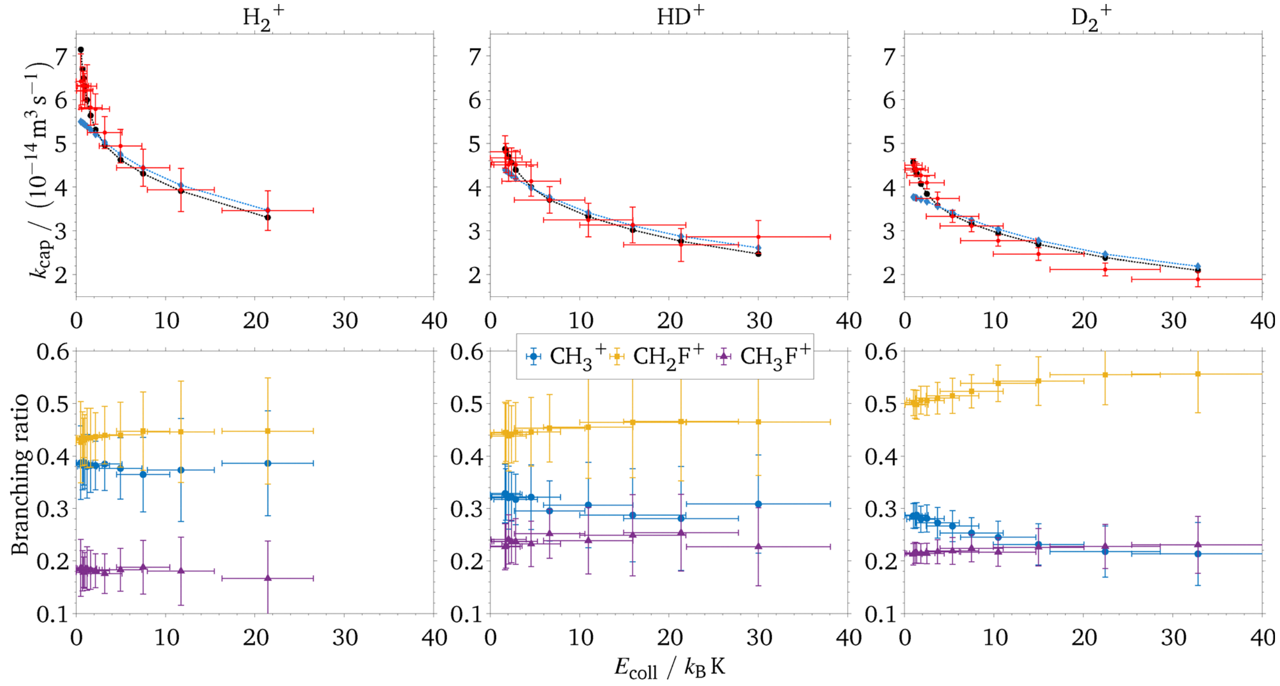

Fig. 4 Top panels: Scaled experimentally observed (red data points with error bars) collision-energy dependence of the total rate coefficient of the reactions between CH_3F and H_2^+ (left), HD^+ (middle) and D_2^+ (right) and corresponding capture rate coefficients calculated with a rotationally adiabatic capture model (black circles, dotted black line) and obtained from classical trajectory simulations (blue diamonds, dotted blue line). The capture rates determined from the rotationally adiabatic capture model and the classical trajectory calculations are convoluted with the experimental collision-energy distribution, see Section 4.3 for details. All model calculations are for T_{rot} = 5 K. Bottom panels: Experimental branching ratios of the individual channels. The vertical error bars represent the statistical uncertainties and the horizontal error bars the square root of the second central moment of the collision-energy distribution.

signals, as a function of the collision energy, which is obtained as the expectation value of the distributions of collision energies $f(E_{\mathrm{coll}})$. Each data point corresponds to the average of a large number of measurements binned according to their collision energy. As explained in Section 2, these ion yields are proportional to the total reaction rate constant. The horizontal error bars represent the standard deviation $s_{E_{\mathrm{coll}}}$ of the collision-energy distribution $f(E_{\mathrm{coll}})$ as shown in Fig. 2 and the vertical error bars represent one standard deviation of all measurements contributing to a given data point.

The experimental data are compared with absolute capture rate constants k_{cap} obtained from classical trajectory calculations (blue diamonds, blue dotted line) as discussed in Section 4.3 and using the rotationally adiabatic capture model (black circles and dotted line) outlined in Section 4.2. Unlike the classical trajectory calculations, the adiabatic-capture-model calculations are performed for a quantum Boltzmann population distribution of the rotational states of CH_3F at a rotational temperature of 5 K, assuming that no *ortho*-to-*para* conversion takes place in the expansion.[73] The calculated rate constants are averaged over the experimentally determined collision-energy distributions $f(E_{\mathrm{coll}})$ to enable comparison. For the comparison, the experimental product-ion yields were multiplied by a global scaling factor (one for each of the reaction systems involving H_2^+, HD^+ and D_2^+) to minimize the respective sums of squared residual deviations from the calculated capture rate coefficients. In all three reaction systems, an increase of the total product-ion yield is observed as the collision energy is reduced towards zero and the overall trend is well described by the calculations, although the classical trajectory calculations underestimate the increase of the rate constants at low collision energies, as discussed in detail in Section 4.3.

The branching ratios corresponding to the formation of CH_3F^+, CH_2F^+ and CH_3^+ are displayed in violet, yellow and blue in the lower panels of Fig. 4. These branching ratios were determined from the integrated intensities of the corresponding mass peaks in the ion-time-of-flight spectra, as explained in Section 2. In all three reaction systems, the dominant product ion is CH_2F^+. The most striking trend in the branching ratios is the decrease of the importance of the CH_3^+ products when H_2^+ (CH_3^+ branching ratio of about 38% at $E_{\mathrm{coll}} \approx k_B \times 25$ K) is successively deuterated to HD^+ (29%) and D_2^+ (22%). In the D_2^+ + CH_3F reaction system, the CH_3^+ product even becomes as weak as the CH_3F^+ product at collision energies beyond $k_B \times 20$ K. The branching ratios also reveal a weak collision-energy dependence, slightly favouring the production of CH_3^+ over the other two product ions at the lowest collision energies. This trend is barely noticeable in the H_2^+ + CH_3F reaction system but increases with increasing degree of deuteration. It thus appears that the smaller the CH_3^+ branching ratio is, the more it increases as the collision energy approaches zero.

All three reaction products (CH_3F^+, CH_2F^+, CH_3^+) can be produced following an initial electron transfer between CH_3F and H_2^+ (HD^+, D_2^+), according to

$$H_2^+ + CH_3F \rightarrow H_2 + CH_3F^+, \tag{5}$$

$$H_2^+ + CH_3F \rightarrow H_2 + [CH_3F^+]^* \rightarrow H_2 + CH_2F^+ + H, \tag{6}$$

and

$$H_2^+ + CH_3F \rightarrow H_2 + [CH_3F^+]^* \rightarrow H_2 + CH_3^+ + F. \tag{7}$$

However, the evolution of the branching ratios with increasing degree of deuteration as well as the opposite trend observed in the collision-energy dependence of the CH_3^+ product branching ratio compared to the CH_2F^+ and CH_3F^+ product branching ratios suggest that electron transfer is not the only mechanism contributing to the formation of CH_3^+. Indeed, to a first approximation, electron transfer is expected to result in very similar distributions of internal energy in CH_3F^+, and thus in very similar fragmentation patterns, for all three reaction systems. Moreover, it seems unlikely that the collision energy would have any influence at all on the product branching ratios of an electron-transfer reaction over the very narrow range ($E_{\mathrm{coll}} < k_B \times 30$ K) studied experimentally. A second mechanism that might contribute to the CH_3^+ product is an F^- atom transfer

$$H_2^+ + CH_3F \rightarrow [H_2\cdots F\cdots CH_3]^+ \rightarrow H + HF + CH_3^+ \tag{8}$$

via a short-range complex. Similarly, an H^- transfer might lead to the production of CH_2F^+

$$H_2^+ + CH_3F \rightarrow [H_2\cdots H\cdots CH_2F]^+ \rightarrow H + H_2 + CH_2F^+. \tag{9}$$

We discuss in the next section how the competition between electron transfer and F^- or H^- atom transfer may be invoked to explain the trends observed in Fig. 4.

4 Discussion

The experimental results presented in Fig. 4 indicate that the CH_3^+, CH_2F^+ and CH_3F^+ products of the $CH_3F + H_2^+$ (HD^+, D_2^+) reaction systems are formed in competing processes, an electron-transfer reaction occurring at intermediate distances (~1 nm, see below) leading to all three products and a short-range reaction that generates either CH_3^+ by F^- transfer or CH_2F^+ by H^- transfer. The corresponding branching ratios η_j for the formation of the different products can therefore be written as

$$\eta_{CH_3^+} = \eta_{ET}p_{CH_3^+} + (1 - \eta_{ET})p'_{CH_3^+} \tag{10}$$

$$\eta_{CH_2F^+} = \eta_{ET}p_{CH_2F^+} + (1 - \eta_{ET})p'_{CH_2F^+} \tag{11}$$

$$\eta_{CH_3F^+} = \eta_{ET}p_{CH_3F^+} + (1 - \eta_{ET})p'_{CH_3F^+} \tag{12}$$

where η_{ET} and $(1 - \eta_{ET})$ represent branching ratios for the electron transfer and the short-range reactions, respectively. $p_{CH_3^+}$, $p_{CH_2F^+}$ and $p_{CH_3F^+}$ are the conditional probabilities that the electron transfer leads to the product ions CH_3^+, CH_2F^+ and CH_3F^+, respectively, and $p'_{CH_3^+}$ and $p'_{CH_2F^+}$ are the conditional probabilities that F^- or H^- is transferred at short range. CH_3F^+ ions can only be produced by electron transfer so that $p'_{CH_3F^+} = 0$ and thus $p'_{CH_2F^+} + p'_{CH_3^+} = 1$.

4.1 Branching ratios for the formation of CH_3F^+, CH_2F^+ and CH_3^+ upon electron transfer

To estimate $p_{CH_3^+}$, $p_{CH_2F^+}$ and $p_{CH_3F^+}$, we model the electron transfer as a sudden, resonant process in which the electron hops from CH_3F molecules in their ground vibronic state and attaches to *ortho*-H_2^+ $X^+\ ^2\Sigma_g^+(v^+ = 0, N^+ = 1)$ (HD^+, *ortho*-D_2^+ $X^+\ ^2\Sigma_g^+$ $(v^+ = 0, N^+ = 0)$) molecules to form neutral H_2 (HD, D_2) in the X $^1\Sigma_g^+$ electronic ground state without transfer of kinetic energy. In this sudden approximation, which also assumes that the CH_3F structure is not strongly perturbed by the ion, the resulting distribution of H_2 (HD, D_2) vibrational levels is given by the Franck–Condon factors $|\langle v^+ = 0|v\rangle|^2$ of the $e^- + H_2^+$ $X^+\ ^2\Sigma_g^+(v^+ = 0) \leftrightarrow X\ ^1\Sigma_g^+(v)$ transition and the energies transferred to CH_3F are given by the corresponding threshold-ionization energies $E_{I,v^+=0\leftarrow v} = hc\tilde{\nu}_{I,0\leftarrow v}$ of CH_3F, as summarized in the upper part of Table 1, see also Fig. 5.

The adiabatic ionization wavenumber of CH_3F is 101 100(10) cm^{-1} (ref. 74 and 75) and, consequently, a sudden, resonant electron transfer forms CH_3F^+ ions with an internal energy $T_{int}(CH_3F^+)$ that rapidly decreases with increasing vibrational excitation of the H_2 product, see third row of the body of Table 1 and Fig. 5. In the sudden approximation, the probability of ionizing CH_3F at $\tilde{\nu}_{I,0\leftarrow v}(H_2)$ corresponds to the intensity $I_{SPES}^{CH_3F}\left(\tilde{\nu}_{I,0\leftarrow v}(H_2)\right)$ of the threshold photoelectron spectrum of CH_3F at the threshold energy corresponding to the $E_{I,v^+=0\leftarrow v}$ ionization energy of H_2 (HD, D_2). The situation is illustrated in Fig. 5, which reproduces the slow photoelectron spectrum (SPES) of CH_3F reported in ref. 60 and gives the positions of the ionization energies of $H_2(v)$, $HD(v)$ and $D_2(v)$ along the upper horizontal bars. The numerical values of $I_{SPES}^{CH_3F}\left(\tilde{\nu}_{I,0\leftarrow v}(H_2)\right)$ obtained after digitalisation of the SPES[60] and normalisation, are listed in the fifth line of Table 1. The probability $p_{0\leftarrow v}$ of the resonant electron transfer

$$H_2^+(v^+ = 0) + CH_3F \rightarrow H_2(v) + CH_3F^+(T_{int}) \qquad (13)$$

can be determined as the normalised product $|\langle v^+ = 0|v\rangle|^2_{H_2}$ $I_{SPES}^{CH_3F}\left(\tilde{\nu}_{I,0\leftarrow v}(H_2)\right)$ and is given in the fifth row of the body of Table 1.

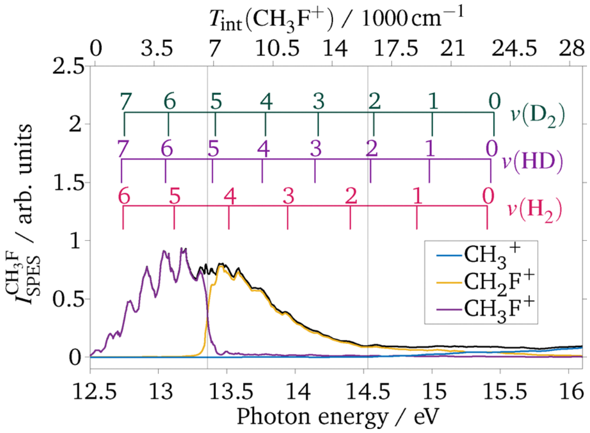

Fig. 5 Mass-resolved threshold photoelectron spectrum of CH_3F reproduced from ref. 60. The black solid line indicates the total intensity $I_{SPES}^{CH_3F}$ and is the sum of the contributions of CH_3F^+ (violet), CH_2F^+ (yellow) and CH_3^+ (blue). The vertical black lines at 13.358 eV and 14.51 eV show the $D_0(CH_2F^+ + H)$ and $D_0(CH_3^+ + F)$ dissociation energies, respectively (upper horizontal scale). The assignment bars above the spectrum show the different threshold ionization energies $hc\tilde{\nu}_{I,0\leftarrow v}$ for $H_2(v)$ (red), $HD(v)$ (violet), $D_2(v)$ (green).

The dissociation energies leading to the fragments $CH_2F^+ + H$ and $CH_3^+ + F$ are 6640(40) cm^{-1} (ref. 62, 66, 74 and 75) and 15 900(160) cm^{-1},[60,62,74,75] respectively, and the corresponding dissociative-ionization thresholds for the formation of $CH_2F^+ + H$ and $CH_3^+ + F$ (at 13.358 eV and 14.51 eV, respectively[60]) are marked by vertical lines in Fig. 5. Below 13.358 eV, the energy is insufficient for the CH_3F^+ ions generated by threshold ionization to fragment. The probability $p_{CH_3F^+}$ for the $H_2^+ + CH_3F$ reaction system can thus be estimated by summing the $p_{0\leftarrow v}$ values in Table 1 for $v = 5$ and $v = 6$ (see Fig. 5; the energy transferred upon production of $H_2(v > 6)$ states is insufficient to ionize CH_3F). When H_2 is formed in the $v = 2$–4 vibrational levels, the product of the electron transfer is mainly CH_2F^+, with only a very minor contribution from CH_3F^+ (see violet trace in Fig. 5). Both CH_3^+ and CH_2F^+ can result from electron-transfer processes forming $H_2(v = 0, 1)$. In these cases, their relative importance corresponds to the ratio of the CH_3^+ and CH_2F^+ ion signals in the mass-selected slow-photoelectron spectra of CH_3F to the total signal $I_{SPES}^{CH_3F}$, as measured by Tang *et al.*[60] and given in the bottom rows of Table 1. Summing the probabilities $p_j = \sum_v p_{0\leftarrow v} p_j(v)$ for the production of $j = CH_3F^+$,

Table 1 Probabilities of forming CH_3F^+, CH_2F^+ and CH_3^+ after a sudden, resonant electron transfer from H_2^+ $X^+\ ^2\Sigma_g^+(v^+ = 0)$ forming H_2 X $^1\Sigma_g^+(v)$. See text for details

	CH_3F^+		CH_2F^+			CH_3^+ and CH_2F^+	
v	6	5	4	3	2	1	0
$\lvert\langle v^+ = 0\rvert v\rangle\rvert^2_{H_2}$	0.001	0.013	0.071	0.209	0.337	0.278	0.091
$\tilde{\nu}_{I,0\leftarrow v}(H_2)/cm^{-1}$	102 764	105 772	109 008	112 471	116 160	120 080	124 236
$T_{int}(CH_3F^+)/cm^{-1}$	1664	4672	7908	11 371	15 060	18 980	23 136
$I_{SPES}^{CH_3F}\left(\tilde{\nu}_{I,0\leftarrow v}(H_2)\right)$	0.271	0.670	0.736	0.387	0.135	0.084	0.091
$p_{0\leftarrow v}$	0.001	0.039	0.239	0.370	0.207	0.107	0.038
$p_{CH_3F^+}(v)$	1.00	1.00	0.04	0.04	0.10	0.09	0.06
$p_{CH_2F^+}(v)$	0.00	0.00	0.96	0.96	0.89	0.74	0.48
$p_{CH_3^+}(v)$	0.00	0.00	0.00	0.00	0.00	0.17	0.46

Table 2 Probabilities for the formation of the three different product ions of the $CH_3F + H_2^+$ (HD^+, D_2^+) reactions produced *via* electron transfer as determined from the slow photoelectron spectrum of CH_3F,[60] see text for details

	$p_{CH_3F^+}$	$p_{CH_2F^+}$	$p_{CH_3^+}$
$CH_3F + H_2^+$	0.10	0.87	0.03
$CH_3F + HD^+$	0.10	0.86	0.04
$CH_3F + D_2^+$	0.13	0.85	0.02

CH_2F^+, or CH_3^+ by the electron-transfer mechanism yields the values listed in the first row of the body of Table 2, where they are compared with the p_j values predicted for the $CH_3F + HD^+$ and $CH_3F + D_2^+$ reaction systems. Tables similar to Table 1 but for the reactions involving HD^+ and D_2^+ are provided in the appendix (Tables 5 and 6). This analysis predicts that electron transfer should lead to a dominant CH_2F^+ product, as observed experimentally, and to a close-to-negligible yield of CH_3^+, which implies that the CH_3^+ ions observed in the ion–molecule reactions are essentially only produced through F^- atom transfer.

A deficiency of this analysis is the underestimation of the yield of CH_3F^+. Indeed, the observed branching ratio for the production of CH_3F^+ is around 20% whereas the predicted branching ratio of ∼10% represents an upper limit for $\eta_{ET} = 1$. This underestimation of the CH_3F^+ yield is the result of the assumption, in the sudden approximation, that no kinetic energy is released upon electron transfer. A non-zero kinetic-energy release upon electron transfer would increase the amount of CH_3F^+ and reduce the amount of CH_3^+ predicted by the sudden approximation even further. When modelling the branching ratios in Sections 4.2.2 and 4.3.2, we therefore assume that $p_{CH_3^+} = 0$. Eqn (10)–(12) can then be simplified to

$$\eta_{CH_3^+} = (1 - \eta_{ET})p'_{CH_3^+} \tag{14}$$

$$\eta_{CH_2F^+} = \eta_{ET}\left(1 - p_{CH_3F^+}\right) + (1 - \eta_{ET})\left(1 - p'_{CH_3^+}\right) \tag{15}$$

$$\eta_{CH_3F^+} = \eta_{ET}p_{CH_3F^+}. \tag{16}$$

4.2 Analysis with the rotationally adiabatic capture model

4.2.1 Capture rate coefficients and their collision-energy dependence. For comparison with the experimental data presented in Fig. 4, we calculate capture rate coefficients using the rotationally adiabatic capture model originally developed by Clary[32] and Troe.[34,36] We follow the procedure described in ref. 41 and determine adiabatic interaction potentials

$$V_L^{JKM}(R) = \overbrace{\frac{L^2}{2\mu R^2} - \frac{\alpha' e^2}{8\pi\varepsilon_0 R^4}}^{V_L} + \Delta E_{\mathrm{Stark}}^{JKM}(R) \tag{17}$$

between the ions (H_2^+, HD^+ and D_2^+, treated as point charges) and CH_3F molecules in the rotational states $|JKM\rangle$. In eqn (17), μ is the reduced mass of the collision, $L^2 = \hbar^2 l(l + 1)$ is the square of the angular momentum of the collision system, R the distance between the H_2^+ (HD^+, D_2^+) ion and CH_3F, α' the polarizability volume of CH_3F (2.54 Å^3)[76,77] and $\Delta E_{\mathrm{Stark}}^{JKM}(R)$ is the rotational-state-specific Stark shift of the $|JKM\rangle$ rotational level of CH_3F in the field of the ion. At the low rotational temperature of CH_3F in the seeded supersonic beam (∼5 K), only rotational levels with $J \leq 2$ and $K = 0, 1$ are significantly populated. Moreover, because the nuclear-spin symmetry is conserved during the supersonic expansion, the Boltzmann factors of excited rotational levels are given with respect to the $J = 0$, $K = 0$ and $J = 1$, $K = 1$ levels for *ortho*- and *para*-CH_3F, respectively. At $T_{rot} = 5$ K, the most populated levels are the $|000\rangle$ (11.3%), $|10M\rangle$ (20.7%) and the $|1{\pm}1M\rangle$ (26.5%) levels. The population of the $|20M\rangle$, $|2{\pm}1M\rangle$ and $|2{\pm}2M\rangle$ levels are 13.0%, 16.6% and 0.4%, respectively.

The Stark shifts of the CH_3F rotational states and the corresponding adiabatic interaction potentials for the $He^+ + CH_3F$ reaction were reported by Zhelyazkova *et al.* (see Fig. 3 of ref. 40). These interaction potentials are practically identical to those for the $D_2^+ + CH_3F$ reaction presented in Fig. 7 because the two reaction systems have almost the same reduced mass. They are easily adapted to obtain the interaction potentials for the $H_2^+ + CH_3F$ and $HD^+ + CH_3F$ system by changing the value of the reduced mass μ in the first term on the right-hand-side of eqn (17).

Within the rotationally adiabatic capture model, the state-specific rate coefficients k^{JKM} are determined from the expression

$$k^{JKM}(E_{\mathrm{coll}}) = v_{\mathrm{rel}}\sigma^{JKM} = v_{\mathrm{rel}}\int_0^{L_{\max}^{JKM}} 2\pi\frac{L}{\mu^2 {v_{\mathrm{rel}}}^2}\mathrm{d}L = \frac{\pi {L_{\max}^{JKM}}^2}{\mu^2 v_{\mathrm{rel}}} \tag{18}$$

where $L_{\max}^{JKM}$ is the maximum value of L for which the barrier [eqn (17)] remains below the collision energy E_{coll}. The state-averaged reaction-rate coefficient is obtained from the state-specific rate coefficients as a weighted sum

$$k(E_{\mathrm{coll}}) = \sum_{JKM} w^{JKM}k^{JKM}(E_{\mathrm{coll}}) \tag{19}$$

over the populated rotational levels of CH_3F, with weights w^{JKM} corresponding to their quantum Boltzmann occupation probability at a rotational temperature $T_{rot} = 5$ K of the CH_3F molecules. As explained in ref. 40, the rate coefficients at low collision energies are dominated by the contributions of the high-field-seeking rotational states, which are subject to negative Stark shifts (see Fig. 3 of ref. 40), *e.g.*, the state $|000\rangle$ and the $J \geq 1$ states with $KM = +J^2$.

The calculated capture rate coefficient $k(E_{\mathrm{coll}})$ is convoluted with the experimentally determined collision-energy distribution $f(E_{\mathrm{coll}})$, leading to the black circles connected by dotted lines in the upper panels of Fig. 4, as already mentioned in Section 3. The results are compared with the experimental data after multiplying these with a global scaling factor. Overall, the calculated capture rate constants are in good agreement with the measurements, confirming the conclusions from studies of an increasing number of ion–molecule reactions that the rotationally adiabatic capture model describes barrier-free exothermic ion–molecule reactions well in the collision-energy range between $\sim k_B \times 1$ K and $k_B \times 50$ K.[41–45]

4.2.2 Collision-energy dependence of the branching ratios.

Calculations based on eqn (18) do not provide information on the branching ratio of different product channels. To describe how the branching ratios depend on the collision energy E_{coll} and on the degree of deuteration of the molecular hydrogen ions, we introduce an expression for the electron-transfer branching ratio η_{ET} within the rotationally adiabatic capture model. We assume that the electron transfer only proceeds in a distance interval $R_{\mathrm{int}} = [R_<, R_>]$ centred below 1 nm with a constant probability across the interval. η_{ET} thus increases with increasing time spent in this interval by the collision partners. This time can be computed, for each value of E_{coll}, from the rotationally adiabatic potentials $V_L^{JKM}(R)$ as the time τ^{JKM} needed for the collision to proceed from the outer limit $R_>$, where the velocity is

$$v_0^{JKM}(L, R_>, E_{\mathrm{coll}}) = \sqrt{2\frac{E_{\mathrm{coll}} - V_L^{JKM}(R_>)}{\mu}}, \tag{20}$$

to the inner limit $R_<$. We determine τ^{JKM} by numerical evaluation of Newton's equations of motion in the potential $V_L^{JKM}(R)$. Assuming an effective R-independent and rotational-state-independent electron-transfer rate constant κ_{eff} in the electron-transfer interval, one obtains the expression

$$P^{JKM}(L, R_<, R_>, E_{\mathrm{coll}}) = 1 - \mathrm{e}^{-\kappa_{\mathrm{eff}}(R_<,R_>)\tau^{JKM}(L,R_<,R_>,E_{\mathrm{coll}})}, \tag{21}$$

for the electron-transfer probability. The value of κ_{eff} is taken to be the same for H_2^+, HD^+ and D_2^+ and is adjusted to best represent the experimental data. With this probability, we compute the electron-transfer cross section σ_{ET} by modifying eqn (18):

$$\sigma_{\mathrm{ET}}^{JKM} = \int_0^{L_{\mathrm{max}}^{JKM}} 2\pi \frac{L P^{JKM}(L, R_<, R_>, E_{\mathrm{coll}})}{\mu^2 v_{\mathrm{rel}}^2} \mathrm{d}L. \tag{22}$$

where $\sigma_{\mathrm{ET}}^{JKM}$ depends on E_{coll}, $R_<$, and $R_>$. Averaging the contributions $\sigma_{\mathrm{ET}}^{JKM}$ over the populated $|JKM\rangle$ states yields σ_{ET}. The branching ratio $\eta_{\mathrm{ET}}^{\mathrm{RACM}}$ for the electron transfer within the rotationally adiabatic capture model is determined as

$$\eta_{\mathrm{ET}}^{\mathrm{RACM}}(E_{\mathrm{coll}}) = \frac{\sigma_{\mathrm{ET}}(E_{\mathrm{coll}})}{\sigma(E_{\mathrm{coll}})} \tag{23}$$

and the rate coefficient for electron transfer is $k_{\mathrm{ET}} = \sigma_{\mathrm{ET}} v_{\mathrm{rel}}$. In sets of calculations performed for different values of $R_>$ and $R_<$, we found that neither the width nor the location of the interval have a significant impact on the resulting value of η_{ET}, because the different values of τ^{JKM} (see eqn (21)) resulting from specific choices of $R_>$ and $R_<$ are compensated by the value of κ_{eff} when κ_{eff} is adjusted to best match the experimental data. For the calculations presented below, we selected $R_< = 0.5$ nm and $R_> = 0.7$ nm, for which we obtained a value of $\kappa_{\mathrm{eff}} = 9.3 \times 10^{12}\ \mathrm{s}^{-1}$.

The full circles in Fig. 6 represent the values obtained for the branching ratio $\eta_{\mathrm{ET}}^{\mathrm{RACM}}(E_{\mathrm{coll}})$ determined in this way as a function of the collision energy. In all three reaction systems, the branching ratio decreases with decreasing collision energy. The reason for this behaviour is that, at low collision energies, the reaction rate is dominated by contributions from high-field-seeking states, and in particular $|(J = 1, 2)KM\rangle$ states with $KM = +J^2$. The attractive internuclear potential accelerates the particles and reduces the time available for the electron transfer and thus the electron-transfer branching ratio decreases.

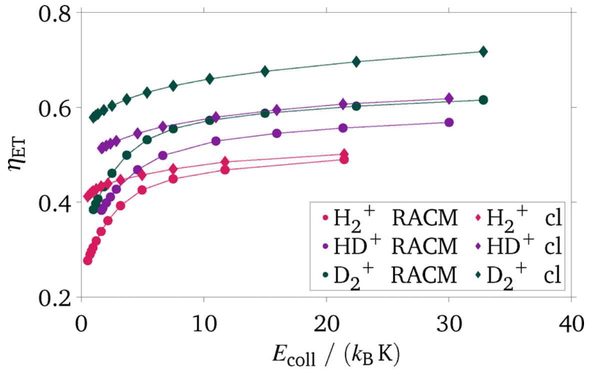

Fig. 6 Electron-transfer branching ratio η_{ET} determined from the rotationally adiabatic capture model (RACM, dots) and the classical trajectory calculations (cl, diamonds) as a function of the collision energy. See text for details.

To compare the experimentally determined values with $\eta_{\mathrm{ET}}^{\mathrm{RACM}}(E_{\mathrm{coll}})$ resulting from eqn (23), we follow the same procedure as used for the total rate coefficients in Section 4.2.1 and convolute $\eta_{\mathrm{ET}}^{\mathrm{RACM}}(E_{\mathrm{coll}})$ with the experimentally determined collision-energy distributions $f(E_{\mathrm{coll}})$. Because $p_{\mathrm{CH_3^+}}$ is assumed to be zero, as explained in Section 4.1, the conditional probabilities of forming CH_3F^+ and CH_2F^+ upon electron transfer are $p_{\mathrm{CH_3F^+}}$ and $(1 - p_{\mathrm{CH_3F^+}})$, respectively. To best represent the experimental data using eqn (14)–(16) we therefore only adjust κ_{eff}, $p_{\mathrm{CH_3F^+}}$ and $p'_{\mathrm{CH_3^+}}$. The results of this analysis are presented in Fig. 9 below (see Section 4.3.2) and the optimal parameter values are listed in Table 3 below.

4.3 Classical trajectory calculations

4.3.1 Capture rate coefficients and their collision-energy dependence.

As an alternative interpretation of the experimental observations, we also carried out classical trajectory simulations based on several simplifying assumptions. The classical trajectories were calculated for a point-like singly positively charged ion approaching a "diatomic" model of CH_3F consisting of point-like CH_3 and F moieties but featuring the electric dipole moment ($\mu_{\mathrm{el}} = 1.857$ D)[78] and electric polarizability volume ($\alpha' = 2.54$ Å^3)[76,77] of CH_3F. The bond between CH_3 and F was modelled as a harmonic oscillator with a wavenumber of 1049 cm^{-1} (ref. 76 and 79) and an equilibrium bond length chosen to reproduce the observed moment of inertia of CH_3F ($I_{\mathrm{b}} = 3.286 \times 10^{-46}$ kg m^2 (ref. 76 and 80)). The initial orientations of CH_3F were sampled isotropically in its equilibrium geometry with rotational angular momenta corresponding to a classical Boltzmann distribution (*i.e.*, disregarding quantum-statistical effects) of vibrational and rotational energy at 5 K. The ion was initialized with an asymptotic velocity determined by the collision energy at a distance of 10 nm with an impact parameter *b*. The trajectories were computed by solving Newton's equations of motion with a constant time step considering only long-range electrostatic interactions (*i.e.*, disregarding short-range repulsion). A trajectory was considered to have led to capture as soon as the change in the ion–molecule separation at any given step became larger than the ion–molecule separation itself. The proportion of captured trajectories $\omega(b)$ was extracted as a function of the sampled impact parameter *b*, which enabled the determination of the capture rate as

$$k_{\mathrm{cap}}^{\mathrm{cl}}(E_{\mathrm{coll}}) = v_{\mathrm{rel}}\int_0^{\infty} 2\pi b\omega(b)\mathrm{d}b = \sqrt{\frac{2E_{\mathrm{coll}}}{\mu}}\sigma_{\mathrm{cap}}^{\mathrm{cl}}(E_{\mathrm{coll}}), \qquad (24)$$

where $\omega(b)$ depends on E_{coll}.

For comparison with the measured capture rate coefficients, the $k_{\mathrm{cap}}^{\mathrm{cl}}$ values calculated at different collision energies were interpolated with a modified Akima method[81,82] as implemented in MATLAB[83] and the resulting function $k_{\mathrm{cap}}^{\mathrm{cl}}(E_{\mathrm{coll}})$ was convoluted with the experimentally determined collision-energy distributions, following the same convolution procedure as for the capture rates calculated using the rotationally adiabatic capture model. The results are plotted as blue diamonds in the top panels of Fig. 4. They are in excellent agreement with both the experimental values and the values calculated with the rotationally adiabatic capture model above $E_{\mathrm{coll}} \approx k_{\mathrm{B}} \times 4$ K. In this range, the classical trajectory and the rotationally adiabatic capture model calculations do not only reproduce the observed trend in the capture rate coefficient but they also give the same quantitative absolute values for $k_{\mathrm{cap}}(E_{\mathrm{coll}})$, which in itself is a remarkable result, given that the classical trajectory simulations do not rely on the assumption of rotationally adiabatic channels. At lower collision energies, however, the classical-trajectory calculations, unlike the rotationally adiabatic capture model, do not reproduce the sharp increase observed experimentally. This difference can unambiguously be attributed to a quantum effect arising from CH_3F molecules in $|JKM\rangle$ rotational levels with $KM = +J^2$ because the diatomic model of CH_3F implies that there is no rotational angular momentum along the symmetric-top axis and quantum-statistical effects are disregarded.

To illustrate this point, the top panels of Fig. 7 depict the adiabatic interaction potentials $V_L^{JKM}(R)$ (see eqn (17)) of the $|JKM\rangle$ states with $J = 0$ and $J = 1$ for the $D_2^+ + CH_3F$ reaction as a function of the ion–molecule separation R for $l = 0$ (full lines) and $l = 70$ (dashed lines). The corresponding state-specific rate coefficients calculated based on the rotationally adiabatic capture model are displayed in the bottom panels of Fig. 7, where they are compared with the rates obtained from the classical trajectory calculations (brown dots). The rate coefficients obtained with the two methods agree for the $K = 0$ case, which is the consequence of representing CH_3F as a diatomic molecule in the classical trajectory calculations, *i.e.*, as a molecule with zero angular momentum ($K = 0$) along the internuclear axis. The interaction potentials and state-specific rate coefficients of the $|JKM\rangle$ levels with $KM = \pm J^2$, which have a nonzero angular-momentum component along the F–CH_3 axis, exhibit a very different behaviour, as already pointed out in ref. 40. The $KM = +J^2$ ($-J^2$) states are associated with strong attractive (repulsive) potentials (see Fig. 7) and their rate coefficients sharply increase (becomes zero) below $E_{\mathrm{coll}} = k_{\mathrm{B}} \times 4$ K. These states are not represented in the classical trajectory calculations and are responsible for the deviations between the rate coefficients calculated with the two methods below $E_{\mathrm{coll}} = k_{\mathrm{B}} \times 4$ K. This difference would persist even at $T_{\mathrm{rot}} = 0$ because the $K = 0$ and $|K| = 1$ rotational levels of CH_3F have different nuclear-spin symmetry and represent the absolute ground states of *ortho*- and *para*-CH_3F, respectively. The simplifying diatomic description of CH_3F in the classical-trajectory simulations is crucial in revealing this effect.

4.3.2 Collision-energy dependence of the branching ratio.

To model the collision-energy dependence of the branching ratios using the classical trajectory simulations, we follow the same procedure as in Section 4.2.2. At every time step along the trajectories, the distance of the centre of mass of CH_3F from the centre of mass of the ion is computed and plotted in a histogram with constant bin width, see Fig. 8. The ordinate values of the histograms in Fig. 8 are obtained from all captured trajectories and thus represent the number of time steps in the entire ensemble of captured trajectories for which the ion–molecule distance lies in an interval corresponding to the relevant bin. Because the duration of a time step is constant, the histograms represent the average time spent in this bin interval by the colliding partners. The branching ratio $\eta_{\mathrm{ET}}^{\mathrm{cl}}$ could therefore in principle be computed as in eqn (21)–(23) using the histogram counts $h(L, R_<, R_>, E_{\mathrm{coll}})$ instead of $\tau^{JKM}(L, R_<, R_>, E_{\mathrm{coll}})$. However, the calculations are carried out by sampling the impact parameter *b*, and therefore also $L = \mu bR$ for every collision energy. The ensemble of trajectories used to generate the histograms thus contains contributions from different *L* values. Rather than sorting the trajectories according to *L* when we compute the electron-transfer probability $P^{JKM}(L, R_<, R_>, E_{\mathrm{coll}})$ (see eqn (21)), it is simpler to first expand $P^{JKM}(L, R_<, R_>, E_{\mathrm{coll}})$ in a Taylor series and truncate the expression after the linear term

$$\begin{aligned} P(L, R_<, R_>, E_{\mathrm{coll}}) &= 1 - \mathrm{e}^{-\kappa_{\mathrm{eff}}^{\mathrm{cl}}(R_<, R_>)h(L, R_<, R_>, E_{\mathrm{coll}})} \\ &\approx \kappa_{\mathrm{eff}}^{\mathrm{cl}}(R_<, R_>)h(L, R_<, R_>, E_{\mathrm{coll}}). \end{aligned} \qquad (25)$$

The branching ratio $\eta_{\mathrm{ET}}^{\mathrm{cl}}$ is then obtained as

$$\begin{aligned} \eta_{\mathrm{ET}}^{\mathrm{cl}} &= \frac{\sigma_{\mathrm{ET}}^{\mathrm{cl}}}{\sigma_{\mathrm{cap}}^{\mathrm{cl}}} \approx \kappa_{\mathrm{eff}}^{\mathrm{cl}}(R_<, R_>)\frac{\int_0^{\infty} 2\pi b\omega(b)h(L, R_<, R_>, E_{\mathrm{coll}})\mathrm{d}b}{\int_0^{\infty} 2\pi b\omega(b)\mathrm{d}b} \\ &= \kappa_{\mathrm{eff}}^{\mathrm{cl}}\tilde{h}(R_<, R_>, E_{\mathrm{coll}}), \end{aligned} \qquad (26)$$

where $\tilde{h}(R_<, R_>, E_{\mathrm{coll}})$ represents the average of *h* over *L* and $\kappa_{\mathrm{eff}}^{\mathrm{cl}}$ is an effective rate constant that is adjusted to best reproduce the experimental data. Fig. 8 depicts the *L*-averaged

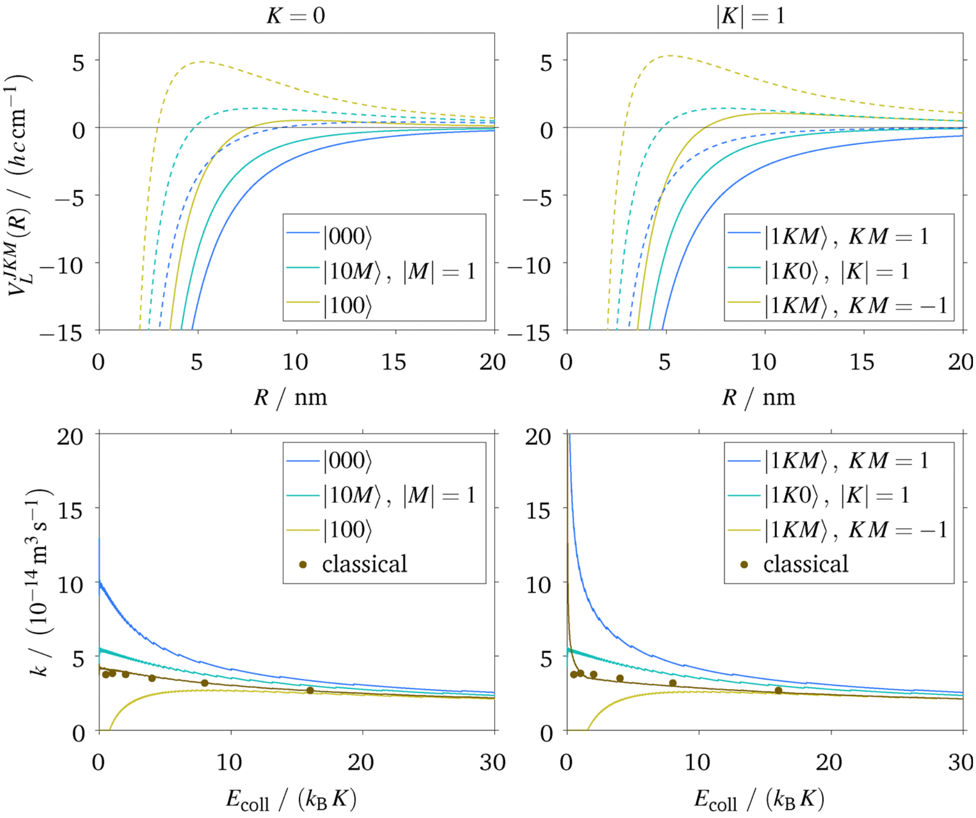

Fig. 7 Top panels: Ion–molecule interaction potentials for the D_2^+ + CH_3F reaction system as defined in eqn (17) for K = 0 (left) and $|K|$ = 1 (right) for l = 0 (full lines) and l = 70 (dashed lines). Bottom panels: Rotational-state-specific reaction rate coefficients for the same system and states. The brown full circles represent the rate coefficients obtained from the classical trajectory calculations and the solid brown line represents the rotational-state-averaged rate coefficient calculated using the rotationally adiabatic capture model for all K = 0 ($K \neq 0$) in the left (right) panel at T_{rot} = 5 K. The ripples in the rate coefficients correspond to the onset of contributions from individual partial waves.

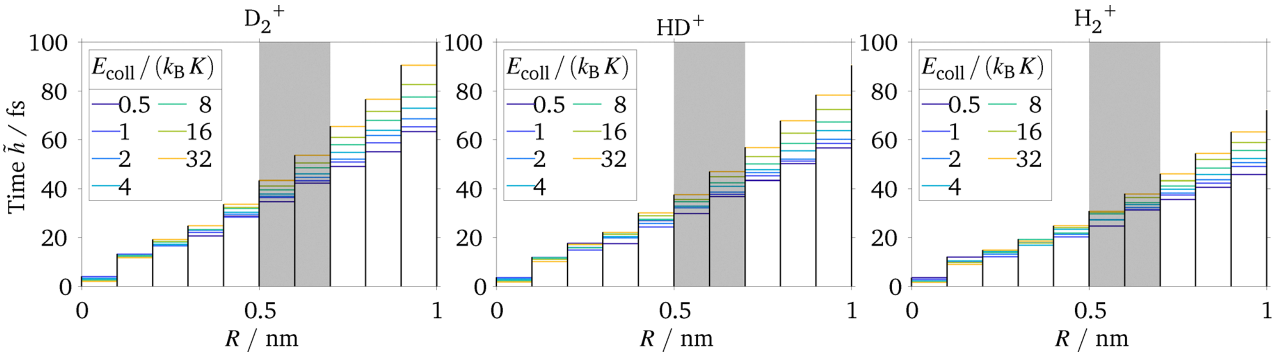

Fig. 8 Histograms showing the average time $\tilde{h}$ spent at the corresponding distance for all captured trajectories. The grey shaded area indicates the R_{int} = [0.5, 0.7] nm range over which $\tilde{h}$ is considered.

histograms corresponding solely to trajectories having led to capture. The grey area in the figure corresponds to the range of R values over which electron transfer was assumed to take place, as in the rotationally-adiabatic-capture-model calculations presented in Section 4.2.2. We verified that the linearisation of $P^{JKM}(L, R_<, R_>, E_{\mathrm{coll}})$ does not significantly modify the results in equivalent calculations performed using the rotationally adiabatic capture model.

The data presented in Fig. 8 follow three main trends: (i) the time spent in the different intervals decreases with decreasing R value because the CH_3F dipole orients toward the charge, which accelerates the motion of the collision partners towards each other. (ii) The time spent by the collision partners in any given R range increases with the degree of deuteration, as expected from the increasing value of the reduced mass and hence the propensity to be accelerated. (iii) The increase with R

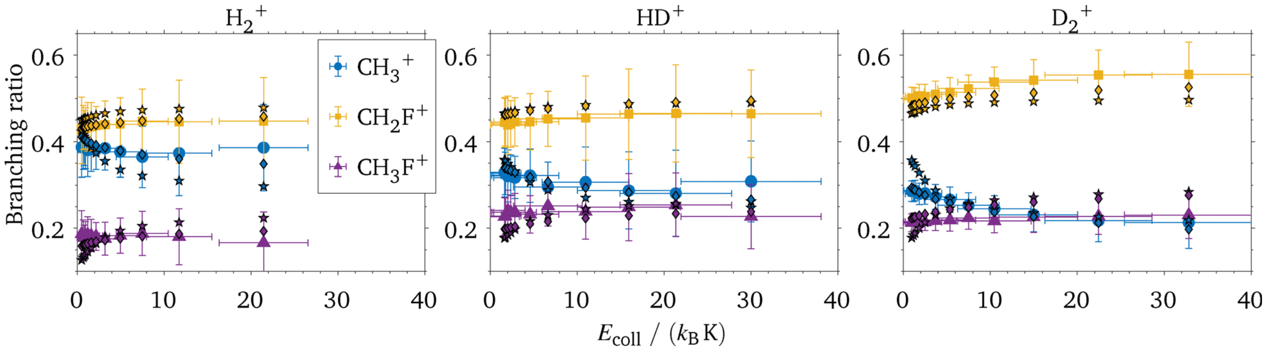

Fig. 9 Experimentally observed collision-energy dependence of the branching ratios of the reactions between CH_3F and H_2^+ (left), HD^+ (middle) and D_2^+ (right). The markers with error bars show the same experimental data as the bottom panels of Fig. 4. The filled stars indicate results from the rotationally adiabatic capture model, and the filled diamonds from the classical trajectory calculations. All model calculations are for T_{rot} = 5 K. See text for details.

of the time spent in the different intervals is weaker at low collision energies than it is at high collision energies. This effect primarily stems from the fact that, at low collision energies, the dipoles start orienting at larger distances, which reduces the time spent at R values larger than 0.3 nm compared to the high-collision-energy situation.

The values of the electron-transfer branching ratio η_{ET}^{cl} obtained from the classical trajectories after interpolation and convolution with the experimental collision-energy distributions are presented as diamonds in Fig. 6, where they can be compared with the corresponding values (dots) determined with the rotationally adiabatic capture model. The electron-transfer branching ratios obtained with both models reveal the same decreasing trend with decreasing collision energies resulting from the dominance, at low collision energies, of contributions from strongly oriented dipoles, as already discussed in Section 4.2.1. The fall of these branching ratios occurs in the range of collision energies where the experimental branching ratios start to change. This region also corresponds to the range where the total rate coefficient increases (see Fig. 4). At the lowest collision energies, the η_{ET} values calculated with the rotationally adiabatic capture model decrease more rapidly than is the case for the values extracted from the classical trajectory calculations. This difference can be attributed to the contribution of the $|JKM\rangle$ states with $KM = +J^2$ which are not included in the classical trajectory calculations, as already discussed in Section 4.3.1. Finally, the η_{ET}^{cl} values are overall slightly larger than the η_{ET}^{RACM} values, and this difference increases with the degree of deuteration.

Fig. 9 compares the CH_3^+, CH_2F^+ and CH_3F^+ branching ratios obtained experimentally (full symbols with error bars) with the branching ratios derived from the rotationally adiabatic capture model (framed stars) and the classical trajectory simulations (framed diamonds), based on the assumption that CH_3^+ is not formed by electron transfer ($p_{CH_3^+} = 0$) and that CH_3F^+ can only be formed by electron transfer $\left(p'_{CH_3F^+} = 0\right)$. Only three parameters were adjusted for each model: $p_{CH_3F^+}$, $p'_{CH_3^+}$ and κ_{eff} and their optimal values are listed in Table 3. The value of κ_{eff} reflects the interval (chosen somewhat arbitrarily) to evaluate the charge-transfer branching ratio, as explained in Section 4.2.2. κ_{eff} is slightly smaller for the classical trajectory simulations than for the rotationally adiabatic capture model. This difference can be explained by the fact that the contribution of the attractive $KM = J^2$ potentials in the latter case reduces the time spent by the collision in the interval $[R_<, R_>]$, which needs to be compensated by a higher κ_{eff} value.

Overall the calculated branching ratios provide a satisfactory description of the observed branching ratios, in particular they qualitatively reproduce the decreasing trend of the CH_2F^+ and CH_3F^+ product branching ratios and the increasing trend of the CH_3^+ branching ratio as the collision energy is reduced below $\sim k_B \times 4$ K. However, the trends predicted by the rotationally adiabatic capture model are stronger than observed experimentally, particularly for the $D_2^+ + CH_3F$ reaction system, indicating possible shortcomings of the capture model calculations. The predictions based on the classical trajectory simulations are closer to the experimental results. However, we demonstrated

Table 3 Parameters obtained from fitting eqn (14)–(16) to the experimentally obtained branching ratios, see Sections 4.2.2 and 4.3.2 for details. RACM stands for rotationally adiabatic capture model

	κ_{eff} [a]	$p_{CH_3F^+}$ [a]	$p_{CH_2F^+}$	$p_{CH_3^+}$ [b]	$p'_{CH_3F^+}$ [c]	$p'_{CH_2F^+}$	$p'_{CH_3^+}$ [a]
RACM	9.3×10^{12} s^{-1}	0.45	0.55	0	0	0.41	0.59
Classical	7.4×10^{12} s^{-1}	0.39	0.61	0	0	0.30	0.70

[a] Adjustable parameter. [b] Fixed to 0 based on the analysis of the electron transfer process presented in Section 4.1. [c] Fixed to 0 because CH_3F^+ can only be formed by charge transfer.

above that this better agreement is the result of the neglect, in the classical trajectory simulations, of rotational angular momentum along the symmetric-top axis and is not physical.

5 Conclusions

The $H_2^+(v^+ = 0)$ + CH_3F reaction and the corresponding reactions of $HD^+(v^+ = 0)$ and $D_2^+(v^+ = 0)$ have been studied at collision energies in the range between 0 and $k_B \times 30$ K and a CH_3F rotational temperature of ∼5 K, at which only the lowest rotational levels with $J \leq 2$ are significantly populated. The measurements focused on the determination of the dependence on the collision energy of the total rate coefficient and the branching ratios for the formation of the different product ions (see Fig. 4). The total rate coefficients of all three reactions were found to increase with decreasing collision energies, particularly below $E_{coll} \approx k_B \times 4$ K. Three product ions were observed: CH_3F^+, CH_2F^+ and CH_3^+. The branching ratios for their formation were found to depend on the collision energy and on the degree of deuteration of the molecular-hydrogen ion. The dominant product is CH_2F^+ but its importance decreases with decreasing collision energy and decreasing degree of deuteration. The second most abundant product is CH_3^+ and its branching ratio follows the exact opposite trends: it increases with decreasing collision energy and degree of deuteration. CH_3F^+ is the least abundant product and its branching ratio is only ∼20% and hardly depends on the degree of deuteration and the collision energy.

To interpret these experimental observations, the ion–molecule capture process was modelled by classical trajectory calculations and by using a rotationally adiabatic capture model inspired by the work of Clary[32] and Troe,[34,36] as described in detail in ref. 40 and 41. The rotationally adiabatic capture model quantitatively reproduces the observed collision-energy dependence of the total rate coefficient in all three reaction systems and demonstrates that the sharp rate-coefficient increase below $E_{coll} = k_B \times 4$ K can be attributed to the reactions involving the high-field-seeking rotational states of CH_3F with $J = 1$, $KM = +1$ (8.8% of the CH_3F population). The classical trajectory calculations were performed for a diatomic-molecule model of CH_3F, *i.e.*, with no angular momentum along the symmetric-top axis to highlight quantum-statistical effects and the effect of the high-field-seeking $K \geq 1$ states by comparison. They quantitatively reproduced the collision-energy dependence of the total rate coefficient down to $E_{coll} = k_B \times 4$ K but failed to account for the sharp rate-coefficient increase observed at the lowest collision energies, thus indirectly confirming the attribution of this increase to CH_3F molecules in $J > 0$, $KM = +J^2$ rotational states made on the basis of the rotationally adiabatic capture model.

All three product ions CH_3F^+, CH_2F^+ and CH_3^+ can be produced following electron transfer from CH_3F to H_2^+, HD^+ or D_2^+. However, modelling the electron transfer as a resonant, sudden process could not explain the observed branching ratios. CH_2F^+ was predicted to be the dominant electron-transfer product, as observed, but the model did not predict any energy dependence of the branching ratios and led to the conclusion that electron transfer hardly produces any CH_3^+ ions at all.

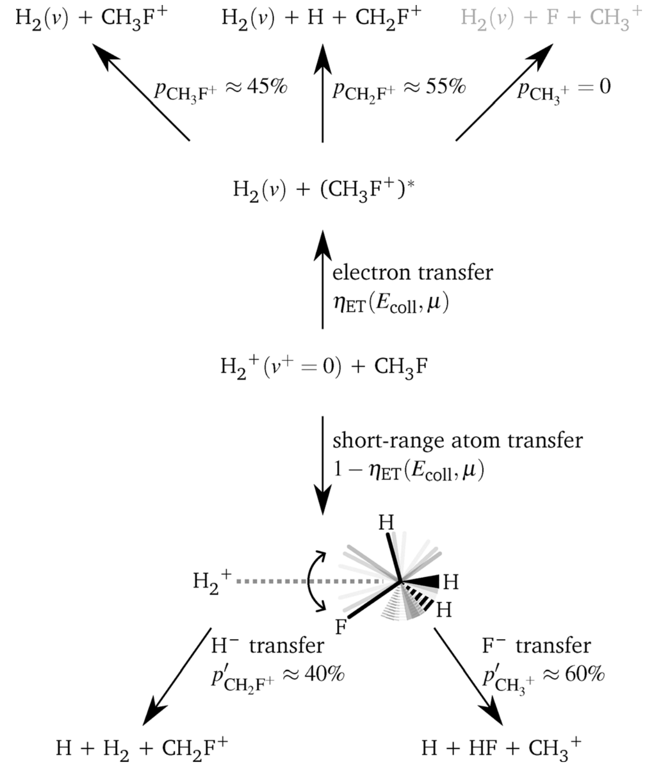

Fig. 10 Overall reaction scheme for the H_2^+ + CH_3F reaction system at low collision energies for the three dominant product channels CH_3F^+, CH_2F^+ and CH_3^+.

A satisfactory interpretation of the experimentally observed branching ratios and their collision-energy dependence could only be reached by invoking competitive kinetics between an electron-transfer pathway yielding only CH_3F^+ and CH_2F^+ and formation of a short-range complex yielding CH_3^+ (and XF + X, with X = H, D) by F^- atom transfer and CH_2F^+ (and XH + X, with X = H, D) by H^- atom transfer. The corresponding overall reaction scheme is presented in Fig. 10 for the H_2^+ + CH_3F reaction system with analogous schemes for HD^+ + CH_3F and D_2^+ + CH_3F.

Because the total rate coefficient can be quantitatively accounted for by the rotationally adiabatic capture model, the electron transfer must take place at ion–molecule separations smaller than the capture radius (which is on the order of a few nm at $E_{coll} = k_B \times 4$ K). The electron transfer is a nonadiabatic process connecting the potential-energy surface associated with the $H_2^+(v^+ = 0)$ + CH_3F reactants with that associated with the CH_3F^+ + $H_2(v)$ products. Assuming that the electron transfer takes place stochastically with a rate κ_{eff} over a selected range of ion–molecule distances, we could explain the dependence of the product-ion branching ratios on the degree of deuteration and on the collision energies. With increasing degree of deuteration, the reduced mass increases and the reactants need more time to reach the short-range complex, thus favouring the longer-range electron-transfer reaction pathway. Similarly, low collision energies favour the reaction of high-field-seeking rotational states of CH_3F ($J > 0$, $KM = +J^2$). These states are associated with strongly attractive ion–molecule interaction potentials and thus with shorter approach times to reach the short-range complex. Consequently, low collision energies favour the F^- and H^- atom-transfer reactions in a short-range complex.

Based on a simplistic stereodynamical argument, with the C–F bond pointing toward the ion, one would expect the ion–molecule approach at short range to favour the formation of CH_3^+ by F^- transfer and to inhibit the formation of CH_2F^+ by H^- transfer. However, at short distances, the C–F bond is not expected to exactly point toward the ion but instead to perform a pendular motion with the classical turning points at a nonzero deviation angle from the internuclear axis (see schematic structure in the lower part of Fig. 10), making H^- transfer possible, though not as likely as the F^- transfer. Considering that at long range the CH_3F molecules in $J = 1$ $K = 1$ states precess around the collision axis at an angle of 45°, it is reasonable to take this angle as representative of the amplitude of the pendular motion at short range. The angle of the C–H bond, *i.e.*, $109° - 45° = 64°$ suggests that the H^- transfer should be possible, although less likely than the F^- transfer (see Fig. 10).

The observed energy-dependent branching ratios could be reproduced semi-quantitatively by fitting only three parameters, the probability $p_{CH_3F^+}$ of forming CH_3F^+ upon electron transfer (∼45%), the probability $p'_{CH_3^+}$ of forming CH_3^+ by short-range F^- transfer (∼60%) and an effective rate constant κ_{eff} for a charge transfer to occur in the range of internuclear separation between 0.5 and 0.7 nm (9.3×10^{12} s^{-1} in Table 3), see Fig. 9. The optimal values of the parameters $p_{CH_3F^+}$ and $p'_{CH_3^+}$ are both greater than 50%, which confirms the expectations from the resonant, sudden electron-transfer model and from the stereodynamical argument concerning the orientation of CH_3F during the approach towards the short-range complex. A full quantitative understanding of the experimental observations would require a careful treatment of the interactions at short range. In this context, progress has been made recently in the case of the electron-transfer reaction between He^+ and CH_3CN[84] through the treatment of the short-range nonadiabatic dynamics. Our results are compatible with the results obtained in ref. 84 in that they show that the approach of the ion and the molecule at low collision energies is restricted to a narrow cone of orientation angles of the symmetric-top axis with respect to the collision axis, and that the charge-transfer rate coefficient can be much smaller than the capture rate coefficient.

We expect that several important aspects of the observed behaviour should be of general validity whenever electron transfer is in competition with adiabatic chemical reactions: (i) the substitution of lighter by heavier isotopes in the reacting ion or molecule should favour electron transfer. (ii) The increasing importance of the high-field-seeking states of the neutral molecule should reduce the importance of electron transfer at low collision energies. (iii) The orientation of the molecule in the field of the ion should finally lead to specific stereodynamical preferences for short-range atom transfer, particularly for low-energy collisions and for reactions involving dipolar molecules, as illustrated here with the example of CH_3F.

Conflicts of interest

There are no conflicts to declare.

Data availability

All relevant data are presented in the article. They can be obtained from the authors upon reasonable request.

Appendices

A Derivation of the collision-energy distribution

This Appendix describes how we determine the collision-energy distribution from measurements of (i) the forward velocity distribution $f_{N_z}(v_N)$ of the neutral CH_3F molecules using fast-ionization gauges and (ii) the three-dimensional velocity distribution $f_{R_x}(v_{R_x})f_y(v_{R_y})f_z(v_{R_z})$ of the Rydberg $H_2(n)$ [$HD(n)$, $D_2(n)$] molecules using imaging and time-of-flight methods. All velocity distributions are well represented by Gaussian distributions and the contributions of the CH_3F molecules to the relative transverse-velocity distribution (x, y) are negligible. We define the probability density functions f as follows

$$f_{N,z}(v_N) = \frac{1}{\sqrt{2\pi\sigma_N{}^2}}\exp\left(-\frac{1}{2}\left[\frac{v_N - \mu_N}{\sigma_N}\right]^2\right) \tag{27}$$

$$f_x(v_{R_x}) = \frac{1}{\sqrt{2\pi\sigma_{R_x}{}^2}}\exp\left(-\frac{1}{2}\left[\frac{v_{R_x}}{\sigma_{R_x}}\right]^2\right) \tag{28}$$

$$f_y(v_{R_y}) = \frac{1}{\sqrt{2\pi\sigma_{R_y}{}^2}}\exp\left(-\frac{1}{2}\left[\frac{v_{R_y}}{\sigma_{R_y}}\right]^2\right) \tag{29}$$

$$f_{R_z}(v_{R_z}) = \frac{1}{\sqrt{2\pi\sigma_{R_z}{}^2}}\exp\left(-\frac{1}{2}\left[\frac{v_{R_z} - \mu_{R_z}}{\sigma_{R_z}}\right]^2\right) \tag{30}$$

where μ_i are the mean velocities with corresponding standard deviations σ_i and $\mu_N - \mu_{R_z} = v^0_{rel}$.

The relative-velocity distribution in the forward (z) direction f_z is given by

$$\begin{aligned} f_z(v_{\mathrm{rel}_z}) &= f_{\mathrm{N},z}(v_\mathrm{N}) * f_{\mathrm{R}_z}(v_{\mathrm{R}_z}) = \int_{-\infty}^{\infty} f_{\mathrm{N},z}(v) f_{\mathrm{R}_z}(-[v_{\mathrm{rel}_z} - v])\mathrm{d}v \\ &= \frac{1}{\sqrt{2\pi({\sigma_\mathrm{N}}^2 + {\sigma_{\mathrm{R}_z}}^2)}} \exp\left(-\frac{1}{2}\frac{\left[v_{\mathrm{rel}_z} - \mu_\mathrm{N} + \mu_{\mathrm{R}_z}\right]^2}{{\sigma_\mathrm{N}}^2 + {\sigma_{\mathrm{R}_z}}^2}\right). \end{aligned} \tag{31}$$

We compute the full three-dimensional velocity distribution f as the product

$$f(v_{\mathrm{R}_x}, v_{\mathrm{R}_y}, v_{\mathrm{rel}_z}) = f_x(v_{\mathrm{R}_x}) f_y(v_{\mathrm{R}_y}) f_z(v_{\mathrm{rel}_z}) \tag{32}$$

$$= \underbrace{\frac{1}{(2\pi)^{\frac{3}{2}}\sqrt{{\sigma_{\mathrm{R}_y}}^2 {\sigma_{\mathrm{R}_x}}^2 ({\sigma_\mathrm{N}}^2 + {\sigma_{\mathrm{R}_z}}^2)}}}_{\chi} \times \exp\left(-\frac{1}{2}\left\{\frac{\left[v_{\mathrm{rel}_z} - v^0_\mathrm{rel}\right]^2}{{\sigma_\mathrm{N}}^2 + {\sigma_{\mathrm{R}_z}}^2} + \frac{{v_{\mathrm{R}_y}}^2}{{\sigma_{\mathrm{R}_y}}^2} + \frac{{v_{\mathrm{R}_x}}^2}{{\sigma_{\mathrm{R}_x}}^2}\right\}\right). \tag{33}$$

To convert the three-dimensional distribution of relative velocities into a (one-dimensional) distribution of the collision energy E_coll, we first transform to spherical coordinates $(v_\mathrm{rel}, \theta, \phi)$

$$\begin{aligned} f(v_\mathrm{rel}, \theta, \phi) &= \chi \exp\left(-\frac{1}{2}\left\{\frac{\left[v_\mathrm{rel}\cos(\theta) - v^0_\mathrm{rel}\right]^2}{{\sigma_\mathrm{N}}^2 + {\sigma_{\mathrm{R}_z}}^2}\right.\right. \\ &\quad \left.\left. + \frac{\left[v_\mathrm{rel}\sin(\theta)\cos(\phi)\right]^2}{{\sigma_{\mathrm{R}_y}}^2} + \frac{\left[v_\mathrm{rel}\sin(\theta)\sin(\phi)\right]^2}{{\sigma_{\mathrm{R}_x}}^2}\right\}\right), \end{aligned} \tag{34}$$

see also Fig. 11.

Next, we exploit the relation

$$f(E_\mathrm{coll})\mathrm{d}E_\mathrm{coll} = \int_0^\pi \int_0^{2\pi} f(v_\mathrm{rel}, \theta, \phi) {v_\mathrm{rel}}^2 \sin(\theta)\mathrm{d}v_\mathrm{rel}\mathrm{d}\theta\mathrm{d}\phi. \tag{35}$$

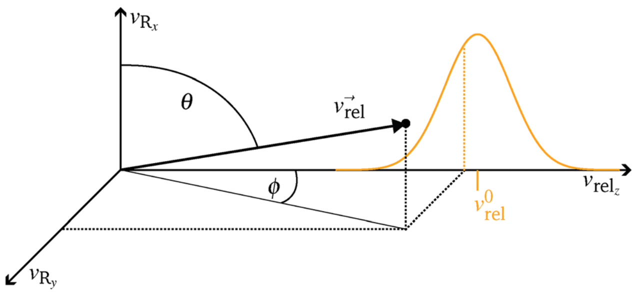

Fig. 11 Example for a point in the three-dimensional relative-velocity space in both Cartesian (v_{R_x}, v_{R_y}, v_{rel_z}) and spherical (v_rel, θ, ϕ) coordinates.

Table 4 Values used to compute the collision-energy distributions displayed in Fig. 12

	S1	S2	S3
μ/amu	3.6	3.6	3.6
v^0_rel/m s^{-1}	13.7	140.3	253.0
σ_N/m s^{-1}	7.9	9.3	11.7
σ_{R_z}/m s^{-1}	41.9	42.8	42.7
σ_{R_y}/m s^{-1}	48.8	54.6	54.9
σ_{R_x}/m s^{-1}	12.0	13.6	14.5

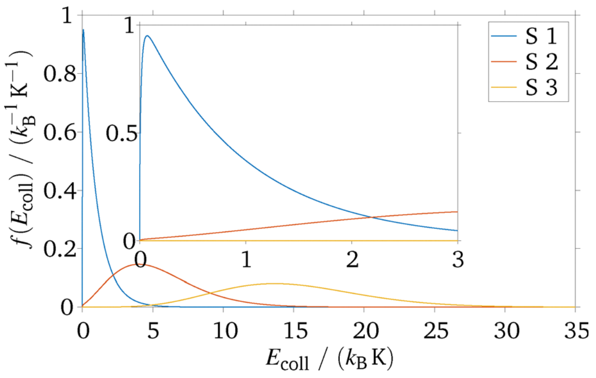

Fig. 12 Collision-energy distributions $f(E_\mathrm{coll})$ for the parameters listed in Table 4.

Expressing the collision energy as

$$E_\mathrm{coll} = \frac{1}{2}\mu {v_\mathrm{rel}}^2, \tag{36}$$

where μ is the reduced mass, the distribution of collision energy is

$$\begin{aligned} f(E_\mathrm{coll}) &= \int_0^\pi \int_0^{2\pi} \frac{1}{\mu}\sqrt{\frac{2E_\mathrm{coll}}{\mu}} \chi \exp\left(-\frac{1}{2}\left\{\frac{\left[\sqrt{\frac{2E_\mathrm{coll}}{\mu}}\cos(\theta) - v^0_\mathrm{rel}\right]^2}{{\sigma_\mathrm{N}}^2 + {\sigma_{\mathrm{R}_z}}^2}\right.\right. \\ &\quad + \frac{\left[\sqrt{\frac{2E_\mathrm{coll}}{\mu}}\sin(\theta)\cos(\phi)\right]^2}{{\sigma_{\mathrm{R}_y}}^2} \\ &\quad \left.\left. + \frac{\left[\sqrt{\frac{2E_\mathrm{coll}}{\mu}}\sin(\theta)\sin(\phi)\right]^2}{{\sigma_{\mathrm{R}_x}}^2}\right\}\right) \sin(\theta)\mathrm{d}\theta\mathrm{d}\phi. \end{aligned} \tag{37}$$

The integrals over the angular variables θ and ϕ are evaluated numerically. For the sample values listed in Table 4, this procedure yields the collision-energy distributions plotted in Fig. 12.

B Tables for the branching-ratio calculation of the reactions of CH_3F with HD^+ and D_2^+

Table 5 Probabilities of forming CH_3F^+, CH_2F^+ and CH_3^+ after a sudden, resonant electron transfer from HD^+ X^+ $^2\Sigma_g^+(v^+ = 0)$ forming HD X $^1\Sigma_g^+(v)$. See text for details

	CH_3F^+		CH_2F^+			CH_3^+ and CH_2F^+		
v	7	6	5	4	3	2	1	0
$\lvert\langle v^+ = 0\vert v\rangle\rvert^2_{HD}$	0.0003	0.004	0.029	0.111	0.248	0.321	0.222	0.063
$\tilde{\nu}_{I,0\leftarrow v}(HD)/cm^{-1}$	102 671	105 269	108 038	110 977	114 087	117 367	120 822	124 454
$T_{int}(CH_3F^+)/cm^{-1}$	1571	4169	6938	9877	12 987	16 267	19 722	23 354
$I^{CH_3F}_{SPES}(\tilde{\nu}_{I,0\leftarrow v}(HD))$	0.222	0.901	0.759	0.571	0.228	0.101	0.087	0.088
$p_{0\leftarrow v}$	0.000	0.019	0.110	0.312	0.277	0.159	0.095	0.027
$p_{CH_3F^+}(v)$	1.00	1.00	0.18	0.04	0.08	0.12	0.08	0.06
$p_{CH_2F^+}(v)$	0.00	0.00	0.82	0.96	0.92	0.86	0.66	0.48
$p_{CH_3^+}(v)$	0.00	0.00	0.00	0.00	0.00	0.02	0.26	0.46

Table 6 Probabilities of forming CH_3F^+, CH_2F^+ and CH_3^+ after a sudden, resonant electron transfer from D_2^+ X^+ $^2\Sigma_g^+(v^+ = 0)$ forming D_2 X $^1\Sigma_g^+(v)$. See text for details

	CH_3F^+		CH_2F^+			CH_3^+ and CH_2F^+		
v	7	6	5	4	3	2	1	0
$\lvert\langle v^+ = 0\vert v\rangle\rvert^2_{D_2}$	0.003	0.019	0.072	0.176	0.277	0.270	0.148	0.035
$\tilde{\nu}_{I,0\leftarrow v}(p - D_2)/cm^{-1}$	102 848	105 446	108 216	111 155	114 264	117 545	121 000	124 632
$T_{int}(CH_3F^+)/cm^{-1}$	1748	4346	7116	10 055	13 164	16 445	19 900	23 532
$I^{CH_3F}_{SPES}(\tilde{\nu}_{I,0\leftarrow v}(D_2))$	0.345	0.873	0.707	0.539	0.222	0.101	0.090	0.090
$p_{0\leftarrow v}$	0.004	0.061	0.189	0.354	0.229	0.102	0.050	0.012
$p_{CH_3F^+}(v)$	1.00	1.00	0.07	0.05	0.07	0.12	0.07	0.04
$p_{CH_2F^+}(v)$	0.00	0.00	0.93	0.95	0.93	0.86	0.66	0.48
$p_{CH_3^+}(v)$	0.00	0.00	0.00	0.00	0.00	0.02	0.27	0.48

Acknowledgements

We thank Hansjürg Schmutz and Josef A. Agner for their technical assistance, Fernanda B. V. Martins and Dr Valentina Zhelyazkova for their contributions to the development of the codes used to calculate the state-specific rate coefficients and for fruitful discussions and Ioana Doran for the Franck–Condon factors of the X^+–X ionizing transitions of hydrogen. This work is supported by the Swiss National Science Foundation (Excellence Grant No. 200020B 200478). TPS acknowledges support from the Leverhulme Trust (EM2022-027).

References

1 V. Wakelam, I. W. M. Smith, E. Herbst, J. Troe, W. Geppert, H. Linnartz, K. Öberg, E. Roueff, M. Agúndez, P. Pernot, H. M. Cuppen, J. C. Loison and D. Talbi, Reaction networks for interstellar chemical modelling: Improvements and challenges, *Space Sci. Rev.*, 2010, **156**, 13–72, DOI: **10.1007/s11214-010-9712-5**.

2 I. W. M. Smith, Laboratory astrochemistry: Gas-phase processes, *Annu. Rev. Astron. Astrophys.*, 2011, **49**, 29–66, DOI: **10.1146/annurev-astro-081710-102533**.

3 M. Jiménez-Redondo, E. Carrasco, V. J. Herrero and I. Tanarro, Isotopic exchange processes in cold plasmas of H_2/D_2 mixtures, *Phys. Chem. Chem. Phys.*, 2011, **13**, 9655–9666, DOI: **10.1039/C1CP20426B**.

4 M. Larsson, W. D. Geppert and G. Nyman, Ion chemistry in space, *Rep. Prog. Phys.*, 2012, **75**, 066901, DOI: **10.1088/0034-4885/75/6/066901**.

5 J. H. Westlake, J. H. Waite, Jr., N. Carrasco, M. Richard and T. Cravens, The role of ion-molecule reactions in the growth of heavy ions in Titan's ionosphere, *J. Geophys. Res.: Space Phys.*, 2014, **119**, 5951–5963, DOI: **10.1002/2014ja020208**.

6 Y.-P. Chang, K. Długołęcki, J. Küpper, D. Rösch, D. Wild and S. Willitsch, Specific chemical reactivities of spatially separated 3-aminophenol conformers with cold Ca^+ ions, *Science*, 2013, **342**, 98–101, DOI: **10.1126/science.1242271**.

7 T. D. Tran, S. Rednyk, A. Kovalenko, Š. Roučka, P. Dohnal, R. Plašil, D. Gerlich and J. Glosík, Formation of H_2O^+ and H_3O^+ cations in reactions of OH^+ and H_2O^+ with H_2: Experimental studies of the reaction rate coefficients from T = 15 to 300 K, *Astrophys. J.*, 2018, **854**, 25, DOI: **10.3847/1538-4357/aaa0d8**.

8 P. Puri, M. Mills, I. Simbotin, J. A. Montgomery Jr., R. Côté, C. Schneider, A. G. Suits and E. R. Hudson, Reaction blockading in a reaction between an excited atom and a charged molecule at low collision energy, *Nat. Chem.*, 2019, **11**, 615–621, DOI: **10.1038/s41557-019-0264-3**.

9 C. R. Markus, O. Asvany, T. Salomon, P. C. Schmid, S. Brünken, F. Lipparini, J. Gauss and S. Schlemmer,

Vibrational excitation hindering an ion-molecule reaction: The c-$C_3H_2^+$-H_2 collision complex, *Phys. Rev. Lett.*, 2020, **124**, 233401, DOI: 10.1103/PhysRevLett.124.233401.

10 B. R. Heazlewood and T. P. Softley, Towards chemistry at absolute zero, *Nat. Rev. Chem.*, 2021, **5**, 125–140, DOI: 10.1038/s41570-020-00239-0.

11 S. Venkataramanababu, A. Li, I. O. Antonov, J. B. Dragan, P. R. Stollenwerk, H. Guo and B. C. Odom, Enhancing reactivity of SiO^+ ions by controlled excitation to extreme rotational states, *Nat. Commun.*, 2023, **14**, 4446, DOI: 10.1038/s41467-023-40135-x.

12 R. Wild, M. Nötzold, M. Simpson, T. D. Tran and R. Wester, Tunnelling measured in a very slow ion-molecule reaction, *Nature*, 2023, **615**, 425–429, DOI: 10.1038/s41586-023-05727-z.

13 M. T. Bowers, *Gas Phase Ion Chemistry*, Academic Press, Cambridge, 1979, DOI: 10.1016/c2013-0-07190-3.

14 C.-Y. Ng, M. Baer, I. Prigogine and S. A. Rice, *State-Selected and State-To-State Ion-Molecule Reaction Dynamics, Part 1. Experiment*, John Wiley & Sons, Inc., New York, 1992, vol. 82, DOI: 10.1002/9780470141397.

15 M. Baer and C.-Y. Ng, *State-Selected and State-To-State Ion-Molecule Reaction Dynamics, Part 2. Theory*, John Wiley & Sons, Inc., New York, 1992, vol. 82, DOI: 10.1002/9780470141403.

16 C.-Y. Ng, State-selected and state-to-state ion-molecule reaction dynamics, *J. Phys. Chem. A*, 2002, **106**, 5953–5966, DOI: 10.1021/jp020055i.

17 N. Bulut, J. Castillo, P. G. Jambrina, J. Kłos, O. Roncero, F. J. Aoiz and L. Bañares, Accurate Time-Dependent Wave Packet Calculations for the $O^+ + H_2 \rightarrow OH^+ + H$ Ion-Molecule Reaction, *J. Phys. Chem. A*, 2015, **119**, 11951–11962, DOI: 10.1021/acs.jpca.5b00815.

18 C. Sanz-Sanz, A. Aguado, O. Roncero and F. Naumkin, Non-adiabatic couplings and dynamics in proton transfer reactions of H_n^+ systems: Application to $H_2 + H_2^+ \rightarrow H + H_3^+$ collisions, *J. Chem. Phys.*, 2015, **143**, 234303, DOI: 10.1063/1.4937138.

19 P. Del Mazo-Sevillano, D. Félix-González, A. Aguado, C. Sanz-Sanz, D.-H. Kwon and O. Roncero, Vibrational, Non-Adiabatic and Isotopic Effects in the Dynamics of the $H_2 + H_2^+ \rightarrow H_3^+ + H$ Reaction: Application to Plasma Modelling, *Mol. Phys.*, 2024, **122**, e2183071, DOI: 10.1080/00268976.2023.2183071.

20 M. Lara, P. G. Jambrina, F. J. Aoiz and J.-M. Launay, Cold and ultracold dynamics of the barrierless $D^+ + H_2$ reaction: Quantum reactive calculations for $\sim R^{-4}$ long range interaction potentials, *J. Chem. Phys.*, 2015, **143**, 204305, DOI: 10.1063/1.4936144.

21 M. Lara-Moreno and T. Stoecklin, Quantum Study of the Radiative Association of $Cl^- + H_2$ and $Cl^- + D_2$, *Eur. Phys. J.-Spec. Top.*, 2023, **232**, 1961–1966, DOI: 10.1140/epjs/s11734-023-00944-z.

22 A. Tsikritea, J. A. Diprose, T. P. Softley and B. R. Heazlewood, Capture theory models: An overview of their development, experimental verification, and applications to ion-molecule reactions, *J. Chem. Phys.*, 2022, **157**, 060901, DOI: 10.1063/5.0098552.

23 L. D. Landau and E. M. Lifshitz, *Quantum mechanics: Non-relativistic theory*, Pergamon Press, Oxford, 3rd edn, 1985.

24 E. E. Nikitin, *Theory of Elementary Atomic and Molecular Processes in Gases*, Clarendon Press, Oxford, 1974.

25 P. Langevin, Une formule fondamentale de théorie cinétique, *Ann. Chim. Phys.*, 1905, **T5**, 245–288.

26 T. Glenewinkel-Meyer and D. Gerlich, Single and merged beam studies of the reaction H_2^+ ($v = 0, 1; j = 0, 4$) + $H_2 \rightarrow H_3^+ + H$, *Isr. J. Chem.*, 1997, **37**, 343–352, DOI: 10.1002/ijch.199700039.

27 T. Oka, Interstellar H_3+, *Chem. Rev.*, 2013, **113**, 8738–8761, DOI: 10.1021/cr400266w.

28 M. Jiménez-Redondo, O. Sipilä, P. Jusko and P. Caselli, Measurements and Simulations of Rate Coefficients for the Deuterated Forms of the $H_2^+ + H_2$ and $H_3^+ + H_2$ Reactive Systems at Low Temperature, *Astron. Astrophys.*, 2024, **692**, A121, DOI: 10.1051/0004-6361/202451757.

29 T. Su and M. T. Bowers, Parameterization of the average dipole orientation theory: Temperature dependence, *Int. J. Mass Spectrom. Ion Phys.*, 1975, **17**, 211–212, DOI: 10.1016/0020-7381(75)85046-7.

30 T. Su and W. J. Chesnavich, Parametrization of the ion-pair molecule collision rate constant by trajectory calculations, *J. Chem. Phys.*, 1982, **76**, 5183–5185, DOI: 10.1063/1.442828.

31 D. C. Clary, D. Smith and N. G. Adams, Temperature dependence of rate coefficients for reactions of ions with dipolar molecules, *Chem. Phys. Lett.*, 1985, **119**, 320–326, DOI: 10.1016/0009-2614(85)80425-5.

32 D. C. Clary, Calculations of rate constants for ion-molecule reactions using a combined capture and centrifugal sudden approximation, *Mol. Phys.*, 1985, **54**, 605–618, DOI: 10.1080/00268978500100461.

33 D. C. Clary, Fast chemical reactions: Theory challenges experiment, *Annu. Rev. Phys. Chem.*, 1990, **41**, 61–90, DOI: 10.1146/annurev.pc.41.100190.000425.

34 J. Troe, Statistical adiabatic channel model for ion-molecule capture processes, *J. Chem. Phys.*, 1987, **87**, 2773–2780, DOI: 10.1063/1.453701.

35 J. Troe, in *State-Selected and State-To-State Ion-Molecule Reaction Dynamics, Part 2. Theory*, ed. C.-Y. Ng and M. Baer, John Wiley & Sons, Inc., 1992, vol. 82 of Adv. Chem. Phys., pp. 485–529, DOI: 10.1002/9780470141403.ch8.

36 J. Troe, Statistical adiabatic channel model for ion-molecule capture processes. II. Analytical treatment of ion-dipole capture, *J. Chem. Phys.*, 1996, **105**, 6249–6262, DOI: 10.1063/1.472479.

37 L. Ploenes, P. Straňák, H. Gao, J. Küpper and S. Willitsch, A novel crossed-molecular-beam experiment for investigating reactions of state- and conformationally selected strong-field-seeking molecules, *Mol. Phys.*, 2021, **119**, e1965234, DOI: 10.1080/00268976.2021.1965234.

38 P. Allmendinger, J. Deiglmayr, O. Schullian, K. Höveler, J. A. Agner, H. Schmutz and F. Merkt, New method to study ion-molecule reactions at low temperatures and application to the $H_2^+ + H_2 \rightarrow H_3^+ + H$ reaction, *ChemPhysChem*, 2016, **17**, 3596–3608, DOI: 10.1002/cphc.201600828.

39 K. Höveler, J. Deiglmayr, J. A. Agner, H. Schmutz and F. Merkt, The H_2^+ + HD reaction at low collision energies: H_3^+/H_2D^+ branching ratio and product-kinetic-energy distributions, *Phys. Chem. Chem. Phys.*, 2021, **23**, 2676–2685, DOI: **10.1039/d0cp06107g**.

40 V. Zhelyazkova, F. B. V. Martins, J. A. Agner, H. Schmutz and F. Merkt, Ion-molecule reactions below 1 K: Strong enhancement of the reaction rate of the ion-dipole reaction He^+ + CH_3F, *Phys. Rev. Lett.*, 2020, **125**, 263401, DOI: **10.1103/PhysRevLett.125.263401**.

41 V. Zhelyazkova, F. B. V. Martins, J. A. Agner, H. Schmutz and F. Merkt, Multipole-moment effects in ion-molecule reactions at low temperatures: Part I – ion-dipole enhancement of the rate coefficients of the He^+ + NH_3 and He^+ + ND_3 reactions at collisional energies E_{coll}/k_B near 0 K, *Phys. Chem. Chem. Phys.*, 2021, **23**, 21606–21622, DOI: **10.1039/d1cp03116c**.

42 V. Zhelyazkova, F. B. V. Martins, M. Žeško and F. Merkt, Multipole-moment effects in ion-molecule reactions at low temperatures: Part II – charge-quadrupole-interaction-induced suppression of the He^+ + N_2 reaction at collision energies below $k_B{\cdot}10$ K, *Phys. Chem. Chem. Phys.*, 2022, **24**, 2843–2858, DOI: **10.1039/D1CP04798A**.

43 F. B. V. Martins, V. Zhelyazkova and F. Merkt, Effects of the charge-dipole and charge-quadrupole interactions on the He^+ + CO reaction rate coefficients at low collision energies, *New J. Phys.*, 2022, **24**, 113003, DOI: **10.1088/1367-2630/ac8a0b**.

44 V. Zhelyazkova, F. B. V. Martins and F. Merkt, Multipole-moment effects in ion-molecule reactions at low temperatures: Part III – the He^+ + CH_4 and He^+ + CD_4 reactions at low collision energies and the effect of the charge-octupole interaction, *Phys. Chem. Chem. Phys.*, 2022, **24**, 16360–16373, DOI: **10.1039/D1CP05861D**.

45 R. Hahn, D. Schlander, V. Zhelyazkova and F. Merkt, Opposite effects of the rotational and translational energy on the rates of ion-molecule reactions near 0 K: the D_2^+ + NH_3 and D_2^+ + ND_3 reactions, *Phys. Rev. X*, 2024, **14**, 011034, DOI: **10.1103/PhysRevX.14.011034**.

46 V. Zhelyazkova, F. B. V. Martins, S. Schilling and F. Merkt, Reaction of an ion and a free radical near 0 K: $He^+ + NO \rightarrow He + N^+ + O$, *J. Phys. Chem. A*, 2023, **127**, 1458–1468, DOI: **10.1021/acs.jpca.2c08221**.

47 E. Vogt and G. H. Wannier, Scattering of ions by polarization forces, *Phys. Rev.*, 1954, **95**, 1190–1198, DOI: **10.1103/PhysRev.95.1190**.

48 I. I. Fabrikant and H. Hotop, Low-energy behavior of exothermic dissociative electron attachment, *Phys. Rev. A:At., Mol., Opt. Phys.*, 2001, **63**, 022706, DOI: **10.1103/PhysRevA.63.022706**.

49 E. I. Dashevskaya, I. Litvin, E. E. Nikitin and J. Troe, Rates of complex formation in collisions of rotationally excited homonuclear diatoms with ions at very low temperatures: Application to hydrogen isotopes and hydrogen-containing ions, *J. Chem. Phys.*, 2005, **122**, 184311, DOI: **10.1063/1.1889425**.

50 E. I. Dashevskaya, I. Litvin, E. E. Nikitin and J. Troe, Relocking of intrinsic angular momenta in collisions of diatoms with ions: Capture of H_2 ($j = 0,1$) by H_2^+, *J. Chem. Phys.*, 2016, **145**, 244315, DOI: **10.1063/1.4972129**.

51 K. Erath-Dulitz, Microwaves Can Suppress Chemical Reactions, *Physics*, 2025, **18**, 63, DOI: **10.1103/Physics.18.63**.

52 M. H. Alexander, E. J. Rackham and D. E. Manolopoulos, Product multiplet branching in the $O(^1D) + H_2 \rightarrow OH(^2\Pi)$ + H reaction, *J. Chem. Phys.*, 2004, **121**, 5221–5235, DOI: **10.1063/1.1779574**.

53 C. E. Dateo and D. C. Clary, Isotopic Branching Ratio for the O^+ + HD Reaction, *J. Chem. Soc., Faraday Trans. 2*, 1989, **85**, 1685, DOI: **10.1039/f29898501685**.

54 M. Chau and M. T. Bowers, Mechanism of Thermal Energy Charge Transfer Reactions: $He^{+\bullet}$, $Ne^{+\bullet}$, $Ar^{+\bullet}$, $Kr^{+\bullet}$, $Xe^{+\bullet}$, $N^{2+\bullet}$, $CO^{+\bullet}$, $CO^{2+\bullet}$, and $N_2O^{+\bullet}$ Reacting with CH_3F, CH_2F_2, CHF_3 and CF_4, *Int. J. Mass Spectrom. Ion Phys.*, 1977, **24**, 191–197, DOI: **10.1016/0020-7381(77)80026-0**.

55 M. Tsuji, T. Funatsu, H. Kouno and Y. Nishimura, Dissociative Charge-Transfer Reactions of Ar^+ with Fluoromethanes at Thermal Energy, *J. Chem. Phys.*, 1992, **97**, 8216–8222, DOI: **10.1063/1.463444**.

56 S. Willitsch, M. T. Bell, A. D. Gingell and T. P. Softley, Chemical applications of laser- and sympathetically-cooled ions in ion traps, *Phys. Chem. Chem. Phys.*, 2008, **10**, 7200–7210, DOI: **10.1039/b813408c**.

57 K. Okada, K. Sakimoto and H. A. Schuessler, Rotational cooling effect on the rate constant in the CH_3F + Ca^+ reaction at low collision energies, *J. Phys. Chem. A*, 2022, **126**, 4881–4890, DOI: **10.1021/acs.jpca.2c01063**.

58 J. Jankunas, B. Bertsche and A. Osterwalder, Study of the $Ne(^3P_2) + CH_3F$ electron-transfer reaction below 1 K, *J. Phys. Chem. A*, 2014, **118**, 3875–3879, DOI: **10.1021/jp502989g**.

59 X. Tang, G. A. Garcia and L. Nahon, CH_3^+ Formation in the Dissociation of Energy-Selected CH_3F^+ Studied by Double Imaging Electron/Ion Coincidences, *J. Phys. Chem. A*, 2015, **119**, 5942–5950, DOI: **10.1021/jp510319b**.

60 X. Tang, G. A. Garcia and L. Nahon, Double Imaging Photoelectron Photoion Coincidence Sheds New Light on the Dissociation of State-Selected CH_3F^+ Ions, *J. Phys. Chem. A*, 2017, **121**, 5763–5772, DOI: **10.1021/acs.jpca.7b06038**.

61 X. Tang, G. A. Garcia and L. Nahon, Dissociation of State-Selected Ions Studied by Fixed-Photon-Energy Double-Imaging Photoelectron Photoion Coincidence: Cases of O_2^+ and CH_3F^+, *Physchem*, 2022, **2**, 261–273, DOI: **10.3390/physchem2030019**.

62 J. Eland, R. Frey, A. Kuestler, H. Schulte and B. Brehm, Unimolecular Dissociations and Internal Conversions of Methyl Halide Ions, *Int. J. Mass Spectrom. Ion Phys.*, 1976, **22**, 155–170, DOI: **10.1016/0020-7381(76)80116-7**.

63 J. Momigny, R. Locht and G. Caprace, Translational Energy Disposal and Mechanisms of Unimolecular Dissociative Photo-Ionization with He(I) and Ne(I) Resonance Lines. A Surprisal Analysis of the $CH_3F \rightarrow CH_3^+ + F$ Process, *Int. J. Mass Spectrom. Ion Phys.*, 1986, **71**, 159–168, DOI: **10.1016/0168-1176(86)85053-4**.

64 R. Locht, J. Momigny, E. Rühl and H. Baumgartel, A Mass Spectrometric Photoionization Study of CH_3F. The CH_2^+,

CH_3^+ and CH_2F^+ Ion Formation, *Chem. Phys.*, 1987, **117**, 305–313, DOI: 10.1016/0301-0104(87)80129-5.

65 I. Torres, R. Martínez and F. Castaño, Electron-Impact Dissociative Ionization of the CH_3F Molecule, *J. Phys. B: At., Mol. Opt. Phys.*, 2002, **35**, 4113–4123, DOI: 10.1088/0953-4075/35/19/313.

66 J. Harvey, R. P. Tuckett and A. Bodi, A Halomethane Thermochemical Network from iPEPICO Experiments and Quantum Chemical Calculations, *J. Phys. Chem. A*, 2012, **116**, 9696–9705, DOI: 10.1021/jp307941k.

67 G. F. Bauerfeldt and H. Lischka, Multireference CI Study of Excitation Energies and Potential Energy Surfaces of CH_3F, *J. Phys. Chem. A*, 2004, **108**, 3111–3118, DOI: 10.1021/jp037091h.

68 H.-W. Xi, M.-B. Huang, B.-Z. Chen and W.-Z. Li, F-Loss and H-Loss Dissociations in Low-Lying Electronic States of the CH_3F^+ Ion Studied Using Multiconfiguration Second-Order Perturbation Theory, *J. Phys. Chem. A*, 2005, **109**, 9149–9155, DOI: 10.1021/jp0524835.

69 S. T. Pratt, J. L. Dehmer, P. M. Dehmer and W. A. Chupka, Reactions of Rydberg states of molecular hydrogen, *J. Chem. Phys.*, 1994, **101**, 882–890, DOI: 10.1063/1.467741.

70 E. Wrede, L. Schnieder, K. Seekamp-Schnieder, B. Niederjohann and K. H. Welge, Reactive scattering of Rydberg atoms: $H^* + D_2 \rightarrow HD + D^*$, *Phys. Chem. Chem. Phys.*, 2005, **7**, 1577–1582, DOI: 10.1039/B417440B.

71 F. B. V. Martins, V. Zhelyazkova, Ch. Seiler and F. Merkt, Cold ion chemistry within a Rydberg-electron orbit: Test of the spectator role of the Rydberg electron in the $He(n) + CO \rightarrow C(n') + O + He$ reaction, *New J. Phys.*, 2021, **23**, 095011, DOI: 10.1088/1367-2630/ac231d.

72 P. Allmendinger, J. Deiglmayr, J. A. Agner, H. Schmutz and F. Merkt, Surface-electrode decelerator and deflector for Rydberg atoms and molecules, *Phys. Rev. A:At., Mol., Opt. Phys.*, 2014, **90**, 043403, DOI: 10.1103/PhysRevA.90.043403.

73 V. Horká-Zelenková, G. Seyfang, P. Dietiker and M. Quack, Nuclear spin symmetry conservation studied for symmetric top molecules (CH_3D, CHD_3, CH_3F, and CH_3Cl) in supersonic jet expansions, *J. Phys. Chem. A*, 2019, **123**, 6160–6174, DOI: 10.1021/acs.jpca.9b02580.

74 M. Grütter, X. Qian and F. Merkt, Photoelectron spectroscopic study of the $E \otimes e$ Jahn-Teller effect in the presence of a tunable spin-orbit interaction. III. Two-state excitonic model accounting for observed trends in the $\tilde{X}^2E$ ground state of CH_3X^+ (X = F, Cl, Br, I) and CH_3Y (Y = O, S), *J. Chem. Phys.*, 2012, **137**, 084313, DOI: 10.1063/1.4745002.

75 S. Gao, Z. Dai, W. Sun, H. Li, J. Wang and Y. Mo, Tunneling splittings in vibronic energy levels of CH_3F^+ ($\tilde{X}^2E$) studied by high resolution photoelectron spectroscopy and ab initio calculation, *J. Chem. Phys.*, 2013, **139**, 064302, DOI: 10.1063/1.4817201.

76 R. D. Johnson III, *NIST Computational Chemistry Comparison and Benchmark Database, NIST Standard Reference Database Number 101 Release 22*, May 2022, https://cccbdb.nist.gov/.

77 T. N. Olney, N. M. Cann, G. Cooper and C. E. Brion, Absolute scale determination for photoabsorption spectra and the calculation of molecular properties using dipole sum-rules, *Chem. Phys.*, 1997, **223**, 59–98, DOI: 10.1016/S0301-0104(97)00145-6.

78 M. D. Marshall and J. S. Muenter, The electric dipole moment of methyl fluoride, *J. Mol. Spectrosc.*, 1980, **83**, 279–282, DOI: 10.1016/0022-2852(80)90051-x.

79 T. Shimanouchi, *Tables of Molecular Vibrational Frequencies, Consolidated Volume I*, National Bureau of Standards Technical Report NBS NSRDS 39, 1972, DOI: 10.6028/NBS.NSRDS.39.

80 D. Papoušek, Y.-C. Hsu, H.-S. Chen, P. Pracna, S. Klee and M. Winnewisser, Far infrared spectrum and ground state parameters of $^{12}CH_3F$, *J. Mol. Spectrosc.*, 1993, **159**, 33–41, DOI: 10.1006/jmsp.1993.1102.

81 H. Akima, A Method of Bivariate Interpolation and Smooth Surface Fitting Based on Local Procedures, *Commun. ACM*, 1974, **17**, 18–20, DOI: 10.1145/360767.360779.

82 H. Akima, A New Method of Interpolation and Smooth Curve Fitting Based on Local Procedures, *J. ACM*, 1970, **17**, 589–602, DOI: 10.1145/321607.321609.

83 The MathWorks Inc., *MATLAB version: 9.13.0.2553342 (R2022b)*, 2022, https://www.mathworks.com.

84 L. Mancini, E. Valença Ferreira de Aragão, F. Pirani, M. Rosi, N. Faginas-Lago, V. Richardson, L. Martini, L. Podio, M. Lippi, C. Codella and D. Ascenzi, Destruction of interstellar methyl cyanide (CH_3CN) *via* collisions with $He^{+\bullet}$ ions, *Astron. Astrophys.*, 2024, **691**, A83, DOI: 10.1051/0004-6361/202451674.